The Astrophysical Journal, 907:29 (18pp), 2021 January 20 https://doi.org/10.3847/1538-4357/abceb6

Resolving the Dust-to-Metals Ratio and CO-to-H_2 Conversion Factor in the Nearby Universe

I-Da Chiang (江宜達)[1], Karin M. Sandstrom[1], Jérémy Chastenet[1], Cinthya N. Herrera[2], Eric W. Koch[3], Kathryn Kreckel[4,5], Adam K. Leroy[6], Jérôme Pety[2,7], Andreas Schruba[8], Dyas Utomo[6,9], and Thomas Williams[4]
[1] Center for Astrophysics and Space Sciences, Department of Physics, University of California, San Diego, 9500 Gilman Drive, La Jolla, CA 92093, USA; idchiang@ucsd.edu
[2] IRAM, 300 rue de la Piscine, F-38406 Saint Martin d'Hères, France
[3] Department of Physics, University of Alberta, 4-183 CCIS, Edmonton, AB T6G 2E1, Canada
[4] Max-Planck-Institut für Astronomie, Königstuhl 17, D-69117 Heidelberg, Germany
[5] Astronomisches Rechen-Institut, Zentrum für Astronomie der Universität Heidelberg, Mönchhofstraße 12-14, D-69120 Heidelberg, Germany
[6] Department of Astronomy, The Ohio State University, 4055 McPherson Laboratory, 140 West 18th Avenue, Columbus, OH 43210, USA
[7] LERMA, Observatoire de Paris, PSL Research University, CNRS, Sorbonne Universités, F-75014 Paris, France
[8] Max-Planck-Institut für extraterrestrische Physik, Giessenbachstraße 1, D-85748 Garching, Germany
[9] National Radio Astronomy Observatory, 520 Edgemont Road, Charlottesville, VA 22903, USA
Received 2020 September 18; revised 2020 November 25; accepted 2020 November 26; published 2021 January 22

Abstract

We investigate the relationship between the dust-to-metals ratio (D/M) and the local interstellar medium environment at ∼2 kpc resolution in five nearby galaxies: IC 342, M31, M33, M101, and NGC 628. A modified blackbody model with a broken power-law emissivity is used to model the dust emission from 100 to 500 μm observed by Herschel. We utilize the metallicity gradient derived from auroral line measurements in H I regions whenever possible. Both archival and new CO rotational line and H I 21 cm maps are adopted to calculate gas surface density, including new wide-field CO and H I maps for IC 342 from IRAM and the VLA, respectively. We experiment with several prescriptions of the CO-to-H_2 conversion factor and compare the resulting D/M–metallicity and D/M–density correlations, both of which are expected to be nonnegative from depletion studies. The D/M is sensitive to the choice of the conversion factor. The conversion factor prescriptions based on metallicity only yield too much molecular gas in the center of IC 342 to obtain the expected correlations. Among the prescriptions tested, the one that yields the expected correlations depends on both metallicity and surface density. The 1σ range of the derived D/M spans 0.40–0.58. Compared to chemical evolution models, our measurements suggest that the dust growth timescale is much shorter than the dust destruction timescale. The measured D/M is consistent with the D/M in galaxy-integrated studies derived from infrared dust emission. Meanwhile, the measured D/M is systematically higher than the D/M derived from absorption, which likely indicates a systematic offset between the two methods.

Unified Astronomy Thesaurus concepts: Interstellar dust (836); Metallicity (1031); Molecular gas (1073); Interstellar dust processes (838); Dust continuum emission (412)

1. Introduction

Dust, the solid grains in the interstellar medium (ISM), plays an important role in shaping the interstellar radiation field and chemistry in the ISM. It absorbs or scatters a significant amount of starlight in galaxies (e.g., 30%; suggested in Bernstein et al. 2002) and reradiates in the infrared (IR; Calzetti 2001; Buat et al. 2012). Dust is important to the formation of molecular clouds because the surfaces of dust grains catalyze the formation of H_2 (Gould & Salpeter 1963; Draine 2003; Cazaux & Tielens 2004; Yamasawa et al. 2011; Galliano et al. 2018), and dust grains can shield gas from the interstellar radiation field and help it cool to the temperature necessary for star formation (Krumholz et al. 2011; Glover & Clark 2012).

In the diffuse ISM of the Milky Way (MW), around 20%–50% of metals reside in dust grains according to elemental depletions ($F_* = 0$–1 in Jenkins 2009). This ratio of total metals locked in solid grains is called the dust-to-metals mass ratio (D/M). The D/M is important to ISM physics and offers constraints on dust chemical evolution. The equilibrium D/M represents a balance between dust formation and dust destruction. Among the dust evolution mechanisms, dust injection from the winds of asymptotic giant branch (AGB) stars, dust production from Type II supernovae (SNe), and dust growth in the ISM are the major mechanisms that increase the D/M, while dust destruction by SN shock waves is the major mechanism that decreases the D/M (Dwek 1998; Lisenfeld & Ferrara 1998; Draine 2009; Zhukovska et al. 2016).

Among these mechanisms, there is a broad consensus that dust growth in the ISM is a critical factor that sets the D/M. Dust growth proceeds by accretion of gas-phase metals in the ISM onto existing dust grains; thus, the dust growth rate should be positively correlated with metallicity and ISM gas density. Several models and simulations show that when the dust growth rate becomes higher than the dust destruction rate, the D/M increases with metallicity and ISM gas density. As dust growth slows down as the gas-phase metals decrease, the D/M becomes roughly constant (Dwek 1998; Hirashita 1999; Inoue 2003; Zhukovska et al. 2008; Asano et al. 2013; Rowlands et al. 2014; Zhukovska 2014; De Vis et al. 2017; Hou et al. 2019; Aoyama et al. 2020).

In addition to dust growth, models show that star formation history (Zhukovska 2014) and the change in dust size distributions (e.g., coagulation and shattering; Hirashita & Kuo 2011; Hirashita & Aoyama 2019; Relaño et al. 2020) also affect the D/M. Simulations also suggest that the resolved D/M is correlated with a galaxy's gas fraction (f_{gas}, the fraction of gas mass to the total gas and stellar mass) and stellar mass distribution (Hou et al. 2019;

Li et al. 2019). Thus, observing the D/M across a range of environments can provide important constraints for dust evolution modeling.

One direct way to constrain the D/M is to observe elemental depletions in the ISM (i.e., the fraction of a given element in dust grains rather than in the gas phase; Jenkins 1987, 1989). Observations in Jenkins (2009) show that depletion increases with the ISM gas density along sight lines within the local part of the MW (distance <10 kpc). This also implies that the D/M varies with ISM environment even when metallicity stays approximately the same. Jenkins & Wallerstein (2017) and Roman-Duval et al. (2019b) also found a varying D/M in the Magellanic Clouds (MCs), where the metallicity is assumed to be approximately constant within each galaxy. These studies also showed that the depletion of dust-forming elements, e.g., silicon and iron, increases with ISM gas surface density.

However, there are several limitations to the depletion observations. Most of them are due to the necessity of obtaining high-resolution UV spectroscopy with a high signal-to-noise ratio (S/N). These limitations include the following: (a) depletions are observable mainly in sight lines with relatively low dust extinction and moderate column densities, (b) depletions are only observable in galaxies where individual stars can be resolved or background quasars can be used, and (c) some key constituents of dust grains, like carbon, are not observable outside the MW due to a lack of current telescope facilities at the necessary wavelengths (Jenkins & Wallerstein 2017; Roman-Duval et al. 2019a, 2019b).

The other common method to determine the D/M is to observe dust mass, gas mass, and metallicity separately and then combine those observations. This method suffers from the combined systematic uncertainties in our understandings from various aspects of ISM physics, but it is still the best strategy we have except direct depletion measurements. The dust mass is usually derived from far-IR (FIR) dust emission or near-IR dust extinction (Hildebrand 1983; Issa et al. 1990; Lisenfeld & Ferrara 1998; Draine & Li 2007; Compiègne et al. 2011; Dalcanton et al. 2015; Jones et al. 2017; Galliano et al. 2018, and references therein), while the gas surface density is derived from gas emission lines like the H I 21 cm (e.g., Walter et al. 2008) and CO rotational lines (e.g., Leroy et al. 2009). Two representative galaxy-integrated surveys using this strategy are Rémy-Ruyer et al. (2014) and De Vis et al. (2019). Rémy-Ruyer et al. (2014) surveyed 126 galaxies and found that the D/M increases with metallicity in galaxies with $12 + \log_{10}(\mathrm{O/H}) < 8.1$ and stays roughly constant in high-metallicity ones. On the other hand, the other survey across ∼500 galaxies by De Vis et al. (2019) showed that the D/M increases with metallicity across the entire observed metallicity range. De Vis et al. (2019) also showed that the D/M correlates with other galaxy properties, e.g., stellar mass, specific star formation rate (SFR), and f_{gas}. The exact dependence of the D/M on galaxy properties remains controversial, which is at least partially a consequence that most of these quantities are mutually correlated.

Since most physical processes that affect the D/M are associated with local ISM environments, spatially resolved D/M studies are necessary for constraining the dust models (Zhukovska 2014; Hu et al. 2019) in addition to measuring a galaxy-integrated D/M. There are several resolved studies targeting single or a few galaxies showing a varying D/M. Roman-Duval et al. (2014, 2017) found that the dust-to-gas ratio (the ratio of dust surface density to total gas surface density, D/G) increases with gas surface density at fixed metallicity in the MCs. Chiang et al. (2018) and Vílchez et al. (2019) found that the D/G increases nonlinearly with metallicity within the nearby spiral galaxy M101. On the other hand, Draine et al. (2014) found a constant D/M in the disk of M31. One problem that emerges in comparing across these studies is the lack of uniformity. Different studies adopted different dust modeling, dust opacity, CO-to-H_2 conversion factors (α_{CO}), and metallicity calibrations. All of these factors together make it hard to compare previous D/M studies on an equal footing.

In addition to uniformity, these factors are also notorious for the level of disagreement among various methodologies. Several studies pointed out that dust opacity may vary. Gordon et al. (2014) and Chiang et al. (2018) showed that the empirical opacity depends on the dust model under the same method of calibration. Dalcanton et al. (2015) and Planck Collaboration et al. (2016) found that the dust mass estimated by the Draine & Li (2007) dust model is ∼two times larger than the dust mass measured by extinction observations, suggesting a possible offset in dust opacity. Fanciullo et al. (2015) estimated that the dust opacity has an ∼20% variation in the typical MW diffuse ISM. Clark et al. (2016, 2019) showed that if the D/M is fixed, dust opacity is inversely correlated with local ISM gas density, spanning a factor of ∼8.

The CO-to-H_2 conversion factor, α_{CO},[10] is known to vary with ISM environment, especially in low-metallicity regions, where the amount of CO-dark H_2 increases as the shielding from dust becomes weaker (Israel 1997; Wolfire et al. 2010; Glover & Mac Low 2011; Leroy et al. 2011; Bolatto et al. 2013; Sandstrom et al. 2013; Hunt et al. 2015; Schruba et al. 2017). Several studies also find that α_{CO} tends to be lower (2–10 times smaller than the disk average value) in the centers of galaxies, possibly due to a stronger CO emission in environments with higher temperature and gas turbulence (Sandstrom et al. 2013; Cormier et al. 2018; Israel 2020). Another problem regarding α_{CO} selection for the purposes of measuring the D/M is that many methods of measuring α_{CO} have built-in assumptions of a fixed D/M or D/G, which would not be self-consistent in studies of D/M variation. For more discussion regarding α_{CO}, we refer our readers to the Bolatto et al. (2013) review and references therein.

To determine metallicity accurately, the electron temperature (T_{e}) of the observed H I region is required. The T_{e} can be derived from temperature-sensitive auroral lines (so-called "direct" measurements; e.g., Berg et al. 2015). However, the auroral lines are rarely used because their intensity is weak and thus hard to observe. The widely used "strong line" measurements make assumptions about T_{e} and therefore have large systematic uncertainties between different calibrations (Kewley & Ellison 2008).

In this work, we measure the spatially resolved D/M–environment relations in five nearby galaxies: IC 342, M31, M33, M101, and NGC 628. This selection is based on their distance and data availability (details in Section 2). By studying the resolved relation between the D/M and local physical quantities across multiple galaxies, we can better constrain our understanding of the dust life cycle. We attempt to overcome the uniformity issues associated with previous studies by using the same calibrations of dust and metals. Moreover, we propose an approach to constrain the D/M and α_{CO} simultaneously.

[10] For the CO-to-H_2 column density conversion factor (X_{CO}), a conversion $X_{\mathrm{CO}} = 2 \times 10^{20}\,\mathrm{cm^{-2}}\,(\mathrm{K\,km\,s^{-2}})^{-1}$ being equivalent to $\alpha_{\mathrm{CO}} = 4.35\ M_{\odot}\ \mathrm{pc^{-2}}\,(\mathrm{K\,km\,s^{-1}})^{-1}$ is used throughout the paper. The masses of helium and heavy elements are included in the α_{CO} factor.

Table 1
Properties of Selected Galaxies[a]

Name	Morph.	Distance[b] (Mpc)	Incl. (deg)	P.A. (deg)	R_{25} (arcmin)
IC 342	SABc	3.45[c]	18.46	…[d]	9.88
M31	Sb	0.79	77.7[e]	38.0[e]	88.9
M33	Sc	0.92	55.0[f]	200.0[f]	31.0
M101	SABc	6.96	18.0[g]	39.0[g]	12.0
NGC 628	Sc	9.77[h]	8.7[i]	20.8[i]	4.94

Notes.
[a] The HyperLeda database (Makarov et al. 2014).
[b] The Extragalactic Distance Database (Tully et al. 2009).
[c] Wu et al. (2014).
[d] Treated as 0°.0 because it is a face-on galaxy.
[e] Corbelli et al. (2010).
[f] Koch et al. (2018).
[g] Sofue et al. (1999).
[h] McQuinn et al. (2017).
[i] Lang et al. (2020).

This paper is presented as follows. We describe our data and dust emission modeling in Section 2. In Section 3, we examine the D/M yielded from existing $\alpha_{\rm CO}$ prescriptions and present a novel approach to constrain the D/M and $\alpha_{\rm CO}$ simultaneously. We discuss the implications and interpretations of our D/M in Section 4. Finally, we present our conclusions in Section 5.

2. Sample and Data

We study the D/M–environment relations in five nearby galaxies, IC 342, M31, M33, M101, and NGC 628. Their properties are tabulated in Table 1. We select these galaxies using the following criteria. (a) They have the photometry data of all five bands in the range $\lambda = 100$–$500\,\mu$m observed by Herschel PACS and SPIRE (Griffin et al. 2010; Pilbratt et al. 2010; Poglitsch et al. 2010), enabling uniform dust modeling. (b) They have both H I and CO maps available. (c) They have metallicity gradients derived from auroral line measurement in H I regions. (d) Their distances are within 10 Mpc, which corresponds to a physical resolution better than 2 kpc at the coarsest-resolution map (SPIRE 500 μm). Note that an exception is made for IC 342 in the metallicity criteria because it has strong line metallicity measurements. We include it because it fits all other criteria. In addition, it spans the high SFR surface density ($\Sigma_{\rm SFR}$), molecular gas surface density ($\Sigma_{\rm mol}$), and gas volume density environments that are not covered by the other galaxies.

We convolve maps from all selected galaxies to a uniform physical resolution using the `astropy.convolution` package (Astropy Collaboration et al. 2013, 2018) and kernels from Aniano et al. (2011). The common resolution for all multiwavelength maps is defined as a Gaussian point-spread function (PSF) with FWHM = 1.94 kpc, which is equivalent to an angular FWHM = 41″ for our most distant galaxy, NCG 628 (here 41″ is the "moderate" Gaussian convolution for our coarsest-resolution data, SPIRE 500; Aniano et al. 2011). After convolution, each map is then reprojected to a grid so that there are 2.5 pixels across the FWHM (i.e., we oversample at roughly the Nyquist sampling rate) using the `astropy`-affiliated package `reproject`.

The IR and UV observations are blended with the cosmic background emission. To remove the background emission in the Herschel maps, we follow the steps in Chiang et al. (2018), which involve a tilted-plane fitting with iterative outlier rejection. For the Wide-field Infrared Survey Explorer (WISE) and Galaxy Evolution Explorer (GALEX) maps, we use the data products from the $z = 0$ Multi-wavelength Galaxy Synthesis (z0MGS; Leroy et al. 2019), which have already been through the background removal process.

To estimate the uncertainties of the observed quantities, we adopt the sensitivities or rms errors from the corresponding reference, multiplied by a factor of $\sqrt{N_f/N_i}$, where N_f and N_i are the numbers of resolution elements after and before convolution, respectively. Whenever there is only rms per channel available in the reference (e.g., H I data in M101), we assume an average gas velocity dispersion $\sigma_{z,\rm gas} = 11\,{\rm km\,s^{-1}}$ (Leroy et al. 2008) to calculate the integrated rms; that is,

$$\mathrm{rms} = (\mathrm{rms\ per\ channel}) \times 2\sqrt{2\ln 2}\ \sigma_{z,\rm gas}, \quad (1)$$

where the $2\sqrt{2\ln 2}$ factor converts $\sigma_{z,\rm gas}$ to FWHM.

We expect most quantities in this work to vary with galactocentric radius. The region above 3σ detection is up to $\sim 0.8R_{25}$. For the galaxy with the largest inclination, M31, the pixels near the minor axis and the center of the galaxy are severely blended with the pixels in the other radial regions after convolution. Thus, we blank the M31 data in the ±45° region around the minor axis. The central $0.4R_{25}$ region of M31 is also blanked due to a lack of metallicity data. The blanked region is shown in Figure 1. All of the surface density (Σ) terms presented in this work are corrected by a factor of $\cos(i)$ to account for inclination. This term will not be shown in the following equations.

2.1. Dust Mass

2.1.1. Herschel FIR Data

We use the $\lambda = 100$–$500\,\mu$m FIR images observed by Herschel PACS and SPIRE (Griffin et al. 2010; Pilbratt et al. 2010; Poglitsch et al. 2010) to derive dust properties. We use the z0MGS data products (Leroy et al. 2019; J. Chastenet et al. 2020, in preparation). The original observations were made by IC 342 (Kennicutt et al. 2011), M31 (Fritz et al. 2012; Groves et al. 2012; Draine et al. 2014), M33 (Kramer et al. 2010; Boquien et al. 2011; Xilouris et al. 2012), M101 (Kennicutt et al. 2011), and NGC 628 (Kennicutt et al. 2011).

The native FWHMs are approximately 7.″0, 11.″2, 18.″2, 24.″9, and 36.″1 for the 100, 160, 250, 350, and 500 μm band images, respectively. We do not include the 70 μm flux because the stochastic heating from small dust grains makes a nonnegligible contribution in that spectral range (e.g., Draine & Li 2007), which is not accounted for by the dust emission model we employ in this study.

2.1.2. Fitting Dust Emission SED

We adopt a modified blackbody model (MBB; Schwartz 1982; Hildebrand 1983) with a broken power-law emissivity to fit the dust emission spectral energy distribution (SED; represented by I_ν) with the 100–500 μm Herschel data. The free parameters in this model are dust surface density (Σ_d), dust temperature (T_d), and the long-wavelength power-law index for emissivity (β_2). This model selection is based on the model comparison in our previous work. In Chiang et al. (2018), we found the broken power-law emissivity MBB to yield a Σ_d that is reasonably below the upper limit derived from metallicity, a

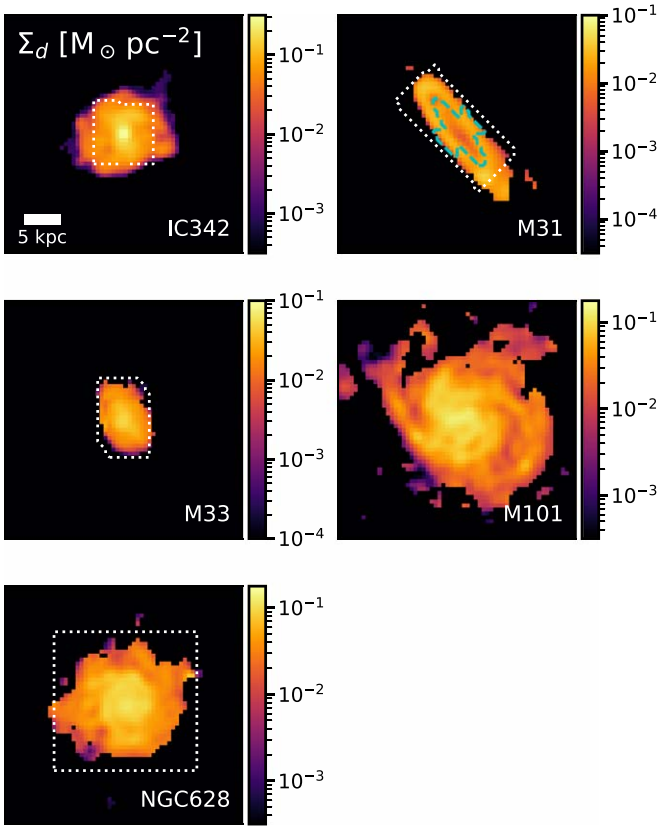

Figure 1. Fitted dust surface densities (Σ_d [$M_\odot$ pc^{-2}]) at the common resolution (a Gaussian PSF with FWHM = 1.94 kpc). The levels of Σ_d are indicated by the color bars attached to each panel. Note that the scales in the panels are not identical. The white dotted line marks the boundary where we have detections in all observations, which we constrain our analysis to. This boundary is defined by CO in most cases. The boundary of M101 is outside the plotting range. The cyan dashed line marks the region removed in M31 due to inclination and lacking metallicity data (see Section 2). The scale bar at the bottom left shows the 5 kpc length for all panels. The dust SED fitting is only performed in regions where S/N > 1 in all five Herschel bands. The region with S/N ⩽ 1 in any of the five Herschel bands appears in black. The >1 dex range in Σ_d within each galaxy indicates that we resolve the exponential disks at this resolution.

T_d gradient matching the dust-heating environment, and one of the best χ^2 value distributions among the five variants of the MBB. In Chiang et al. (2018), we have shown that the Σ_d derived with an MBB with a broken power-law emissivity is within 0.1 dex of the Σ_d derived with the commonly used MBB with a constant power-law emissivity (β fixed at 2.0).

The MBB model takes the form

$$I_\nu(\lambda)[\mathrm{MJy\ sr^{-1}}] = \kappa(\lambda)\Sigma_d\, B_\nu(\lambda, T_d), \tag{2}$$

where $\kappa(\lambda)$ is the wavelength-dependent emissivity, and $B_\nu(\lambda, T_d)$ is the blackbody SED at dust temperature T_d. We adopt a broken power-law emissivity (Gordon et al. 2014; Chiang et al. 2018; also see Reach et al. 1995), described by

$$\kappa(\lambda) = \begin{cases} \kappa_{160}\left(\frac{\lambda_0}{\lambda}\right)^\beta & \text{for} \quad \lambda < \lambda_b \\ \kappa_{160}\left(\frac{\lambda_0}{\lambda_b}\right)^\beta \left(\frac{\lambda_b}{\lambda}\right)^{\beta_2} & \text{for} \quad \lambda \geqslant \lambda_b \end{cases}, \tag{3}$$

where λ_b is the break wavelength fixed at 300 μm and β is the short-wavelength power-law index fixed at 2.0; the long-wavelength power-law index (β_2) is left as a free parameter in the fitting[11]; and $\lambda_0 = 160\,\mu$m is the reference wavelength for $\kappa(\lambda)$.

The reference emissivity κ_{160} is calibrated with the depletion measurements and FIR SED in the MW cirrus (Jenkins 2009; Gordon et al. 2014). The calibrated value for our model is $\kappa_{160} = 20.73 \pm 0.97\,\mathrm{cm^2\,g^{-1}}$ (Chiang et al. 2018). This calibration method is known to produce Σ_d values not exceeding the upper bound given by the local available metals (Gordon et al. 2014; Chiang et al. 2018).

We fit the dust SED in all pixels with S/N > 1 in all five Herschel bands following the grid-based fitting method presented in Gordon et al. (2014) and Chiang et al. (2018). We build a multidimensional grid with each grid point representing a combination of possible model parameters. At each pixel of the maps, we calculate the likelihood that a given model fits the observations and repeat at all grid points. Finally, we compute the expectation values of the model parameters. The likelihood is calculated with a covariance matrix consisting of both the variance of each band and the band-to-band covariance. This method allows us to directly account for the band-to-band correlation due to noise from astronomical sources, e.g., background galaxies and MW cirrus, which dominate the FIR background noise. For more details, we refer to Section 3.2 of Chiang et al. (2018) or Section 4 of Gordon et al. (2014).

The fitting is done at the common resolution. Figure 1 shows the resulting dust maps. Although the angular resolution has been degraded substantially for some galaxies, the range of Σ_d at the common resolution is still more than 1 order of magnitude in each galaxy. This indicates that the ∼2 kpc resolution resolves the exponential disks of our selected galaxies.

2.1.3. Fitting Errors

For each model parameter ($X = \log_{10}\Sigma_d$, T_d, or β_2), we use the marginalized likelihood-weighted 16th and 84th percentile (X_{16} and X_{84}, respectively) at each pixel to represent the $1-\sigma$ distribution. We then quote the maximum difference between the expectation value ($X_{\rm exp}$) and the $1-\sigma$ distribution as the fitting error ϵ_X, that is,

$$\epsilon_X = \max((X_{84} - X_{\rm exp}), (X_{\rm exp} - X_{16})). \tag{4}$$

This is the same method as in Chiang et al. (2018).

2.2. Gas Masses

We calculate the total gas surface density ($\Sigma_{\rm gas}$) as

$$\Sigma_{\rm gas} = \Sigma_{\rm atom} + \Sigma_{\rm mol}, \tag{5}$$

where $\Sigma_{\rm atom}$ is the atomic gas surface density and $\Sigma_{\rm mol}$ is the molecular gas surface density.

2.2.1. Atomic Gas Mass

We use new and archival H I 21 cm line emission ($I_{\rm H\,I}$) data to trace $\Sigma_{\rm atom}$. The data sources are IC 342 (PI: K.M. Sandstrom; I. Chiang et al. 2020, in preparation),[12] M31 (Braun et al. 2009), M33 (Koch et al. 2018), M101 (Walter et al. 2008), and NGC

[11] In this work, the fitted β_2 spans the 1σ range of $2.09^{+0.16}_{-0.22}$, $1.81^{+0.12}_{-0.29}$, $1.25^{+0.23}_{-0.26}$, $1.44^{+0.52}_{-0.42}$, and $1.84^{+0.28}_{-0.38}$ in IC 342, M31, M33, M101, and NGC 628, respectively. The overall 1σ range is $1.64^{+0.43}_{-0.50}$.

[12] Observed with the VLA.

628 (Walter et al. 2008). The resolution of the H I data is high enough that it never limits our analysis. For M31 and M33, the two galaxies with the largest angular scales, a short-spacing correction with Green Bank Telescope data has been included in the original works (Braun et al. 2009; Koch et al. 2018). The short-spacing correction is not applied in IC 342, M101, and NGC 628.

Among these three galaxies, IC 342 is most likely to have its $I_{\rm H\,I}$ underestimated with interferometric data only due to its sky coverage; the H I 21 cm signal in IC 342 spans a diameter of $\sim 45'$, whereas the largest angular scale covered by the Karl G. Jansky Very Large Array (VLA) D configuration is $\sim 16'$ in the L band. The total atomic mass in our IC 342 map is $M_{\rm atom} = 7.9 \times 10^9\,M_\odot$, which is close to the $M_{\rm atom} = 8.4 \times 10^9\,M_\odot$ in Crosthwaite et al. (2000; distance corrected). Single-dish measurements in the literature (Rots 1979; distance corrected) showed $M_{\rm atom} = 18.7 \times 10^9\,M_\odot$. However, this value is expected to be overestimated because the low spatial and velocity resolutions in the Rots (1979) data are not enough to distinguish and remove the MW foreground completely.

We also compare our result with the recent single-dish data (EBHIS; Kerp et al. 2011; Winkel et al. 2016). We choose a spectral range that is free from the MW foreground, $\sim$43–128 km s^{-1} (the H I 21 cm signal in IC 342 spans $\Delta v \sim 210$ km s^{-1}). We find that the total flux from EBHIS data is $\sim$1.6 times larger than our VLA measurement in this range, which indicates that a short-spacing correction is desired but confused by MW foreground emission. Since this 1.6 factor is an average value instead of an offset that can be directly applied to all pixels, we do not include it in our analysis. This factor does not affect our main conclusions due to the low atomic gas content in our region of interest, which is at the center of IC 342.

We calculate $\Sigma_{\rm atom}$ from $I_{\rm H\,I}$ via the following equation, assuming the opacity is negligible (e.g., Walter et al. 2008):

$$\Sigma_{\rm atom}\,[M_\odot\,{\rm pc}^{-2}] = 1.36 \times (8.86 \times 10^3) \times \left(\frac{I_{\rm H\,I}\,[{\rm Jy\,beam^{-1}\,km\,s^{-1}}]}{B_{\rm maj}\,[''] \times B_{\rm min}\,['']}\right), \quad (6)$$

where $B_{\rm maj}$ and $B_{\rm min}$ are the FWHM of the major and minor axes of the synthesized beam, respectively. The 1.36 factor accounts for the mass of helium and heavy elements.

2.2.2. Molecular Gas Mass

We use CO rotational line emission ($I_{\rm CO}$) to trace $\Sigma_{\rm mol}$. The data sources are IC 342 (A. Schruba et al. 2020, in preparation),[13] M31 (Nieten et al. 2006), M33 (Gratier et al. 2010; Druard et al. 2014), M101 (Leroy et al. 2009), and NGC 628 (Leroy et al. 2009). The CO resolution is high enough that it never limits our analysis.

Throughout the paper, $\alpha_{\rm CO}$ is quoted for the CO $J = 1 \rightarrow 0$ rotational line at 115 GHz and includes a factor to account for helium. However, we use the 230 GHz CO $J = 2 \rightarrow 1$ data in M33, M101, and NGC 628. In those cases, we quote a (2–1)/(1–0) brightness temperature ratio (R_{21}) to convert the integrated intensity, that is,

$$I_{{\rm CO}\,J\,=\,1\rightarrow 0}\,[{\rm K\,km\,s^{-1}}] = \frac{I_{{\rm CO}\,J\,=\,2\rightarrow 1}\,[{\rm K\,km\,s^{-1}}]}{R_{21}}. \quad (7)$$

We use $R_{21} = 0.8$ in M33 (Gratier et al. 2010; Druard et al. 2014) and $R_{21} = 0.7$ in M101 and NGC 628 (Leroy et al. 2013). We do not include uncertainties resulting from variations of R_{21} in the analysis. The uncertainty in the D/M due to the choice of R_{21} is $\leqslant$0.05 dex in the three galaxies using CO $J = 2 \rightarrow 1$ data (M33, M101, and NGC 628). In M33 and NGC 628, the measured variations of R_{21} are reasonably small (Sandstrom et al. 2013; Druard et al. 2014). In M101, R_{21} could increase by $\sim$0.3 dex in the central $\sim$0.05 R_{25} ($\sim$1.2 kpc; Sandstrom et al. 2013), which indicates that we might underestimate $\Sigma_{\rm mol}$ in that small region. The R_{21} values adopted in this study are consistent with the Physics at High Angular resolution in Nearby GalaxieS (PHANGS) survey measurements ($R_{21} = 0.64 \pm 0.09$; J. den Brok et al. 2020, in preparation) considering the systematic uncertainties due to calibration (e.g., 15% for CO $J = 2 \rightarrow 1$ data in Druard et al. 2014).

We can translate $I_{\rm CO}$ to $\Sigma_{\rm mol}$ via a CO-to-H_2 conversion factor ($\alpha_{\rm CO}$):

$$\Sigma_{\rm mol}\,[M_\odot\,{\rm pc}^{-2}] = \alpha_{\rm CO}\,[M_\odot\,{\rm pc}^{-2}\,({\rm K\,km\,s^{-1}})^{-1}] \times I_{{\rm CO}\,J=1\rightarrow 0}\,[{\rm K\,km\,s^{-1}}]\ . \quad (8)$$

Since the D/M is sensitive to the choice of $\alpha_{\rm CO}$, we calculate our results with four $\alpha_{\rm CO}$ prescriptions in this study (see Table 2). The conventional MW $\alpha_{\rm CO}$ ($\alpha_{\rm CO}^{\rm MW}$; Solomon et al. 1987; Strong & Mattox 1996; Abdo et al. 2010) is one of the most widely used choices for $\alpha_{\rm CO}$. It has a fixed value of 4.35 $M_\odot$ pc^{-2} (K km s^{-1})$^{-1}$ and no dependence on the environments (see footnote [10] for the conversion between $\alpha_{\rm CO}$ and $X_{\rm CO}$). The Schruba et al. (2012, their Table 7; the "all galaxies" formula with the HERACLES sample) prescription ($\alpha_{\rm CO}^{\rm S12}$) models $\alpha_{\rm CO}$ as a simple power law with metallicity, which is a common strategy in modeling $\alpha_{\rm CO}$ (e.g., Israel 1997; Feldmann et al. 2012; Hunt et al. 2015; Accurso et al. 2017). Here $\alpha_{\rm CO}^{\rm S12}$ has the largest normalization factor among the prescriptions; thus, it results in the overall highest $\Sigma_{\rm gas}$ or the smallest D/M. Another power-law prescription we include here is the Hunt et al. (2015, Section 5.1) prescription ($\alpha_{\rm CO}^{\rm H15}$), which is a power law with metallicity in regions below solar metallicity ($Z_\odot$) and a constant at $\alpha_{\rm CO}^{\rm MW}$ above $Z_\odot$. This cutoff is due to a smaller amount of CO-dark H_2 at high metallicity. The Bolatto et al. (2013, Equation (31)) prescription ($\alpha_{\rm CO}^{\rm B13}$) has an exponential

Table 2
List of $\alpha_{\rm CO}$ Prescriptions Used in This Work

Prescription	$\alpha_{\rm CO}$ Formula $[M_\odot\,{\rm pc}^{-2}\,({\rm K\,km\,s^{-1}})^{-1}]$
$\alpha_{\rm CO}^{\rm MW}$	4.35
$\alpha_{\rm CO}^{\rm S12}$	$8.0 \times (Z/Z_\odot)^{-2.0}$
$\alpha_{\rm CO}^{\rm B13}$	$2.9 \times \exp\left(\frac{0.4}{Z/Z_\odot}\right) \times \begin{cases} (\Sigma_{\rm Total}^{100})^{-0.5} & ,\Sigma_{\rm Total}^{100} \geqslant 1 \\ 1 & ,\Sigma_{\rm Total}^{100} < 1 \end{cases}$
$\alpha_{\rm CO}^{\rm H15}$	$4.35 \times \begin{cases} 1 & ,Z \geqslant Z_\odot \\ (Z/Z_\odot)^{-1.96} & ,Z < Z_\odot \end{cases}$

Note. Throughout this paper, $\Sigma_{\rm Total}^{100}$ is $\Sigma_{\rm Total}$ in 100 $M_\odot$ pc^{-2}, and $Z/Z_\odot = 1$ at $12 + \log_{10}({\rm O/H}) = 8.69$.

[13] Observed with the NOrthern Extended Millimeter Array (NOEMA) and the IRAM 30 m telescope.

Table 3
$12 + \log_{10}(O/H)$ Data

Name	Reference	$12 + \log_{10}(O/H)$ at the Galaxy Center (dex)	Slope[a]	
			(dex kpc^{-1})	(dex R_{25}^{-1})
IC 342	K. Kreckel et al. (2020, in preparation)[b]	8.64 (±0.01)	−0.012 (±0.003)	−0.12 (±0.03)
M31	Zurita & Bresolin (2012)	8.72 (±0.18)	−0.026 (±0.013)	−0.52 (±0.26)
M33	Bresolin (2011)	8.50 (±0.02)	−0.041 (±0.005)	−0.34 (±0.04)
M101	Croxall et al. (2016); Berg et al. (2020)	8.78 (±0.04)	−0.031 (±0.002)	−0.75 (±0.06)
NGC 628	Berg et al. (2015, 2020)	8.71 (±0.06)	−0.027 (±0.007)	−0.38 (±0.10)

Notes.
[a] The slopes have been converted to account for the distances and R_{25} values adopted in this paper.
[b] Using the S calibration from PG16S.

dependence on metallicity and a power-law dependence on total surface density ($\Sigma_{\rm Total} = \Sigma_{\rm gas} + \Sigma_\star$) in the regions with the highest surface densities. Note that we assume $\Sigma_{\rm GMC} = 100\,M_\odot\,{\rm pc}^{-2}$ in the $\alpha_{\rm CO}^{\rm B13}$ case.

2.3. Metallicity

We use the oxygen abundance, $12 + \log_{10}(O/H)$, to trace metallicity in this work. We adopt $12 + \log_{10}(O/H)_\odot = 8.69$ (Asplund et al. 2009). We adopt measurements from multiple sources (Table 3). We use gradients of $12 + \log_{10}(O/H)$ derived from auroral line measurements in H I regions in all galaxies except IC 342. For IC 342, we use the S calibration for strong lines from Pilyugin & Grebel (2016, hereafter PG16S), which is a calibration showing good agreement with direct metallicity measurements (Croxall et al. 2016; Kreckel et al. 2019). Within the region of interest in this work, the $12 + \log_{10}(O/H)$ ranges from 8.2 to 8.8. Note that in M31, the metallicity gradient is derived with data outside $0.4R_{25}$ only (Zurita & Bresolin 2012); thus, we blank all M31 data within $0.4R_{25}$ in the D/M analysis.

In the calculation of the D/M, we need to convert $12 + \log_{10}(O/H)$ to metallicity ($Z = \Sigma_{\rm metal}/\Sigma_{\rm gas}$; note that $\Sigma_{\rm gas}$ includes the mass of heavy elements in our notation) because a complete measurement of the abundance of all elements is unavailable. We use a fixed oxygen-to-metals ratio, $M_O/M_{\rm metal} = 0.51$, calculated from the solar neighborhood chemical composition (Lodders 2003). The complete conversion is

$$Z = \frac{1}{M_O/M_{\rm metal}}\frac{m_O}{1.36\,m_H}10^{(12+\log_{10}(O/H))-12}, \quad (9)$$

where m_O and m_H are the atomic masses for oxygen and hydrogen, respectively; the 1.36 factor converts hydrogen mass to total gas, which is consistent with the conversion in Section 2.2. We do not include a correction of [O/H] due to depletion of oxygen in H I regions, which is estimated to be $\lesssim$0.1 dex (Esteban et al. 1998; Peimbert & Peimbert 2010).

Although we do our best to quote the most reliable metallicity, we would like to remind readers of two remaining caveats in our methodology. (a) A fixed oxygen-to-metals ratio across all ISM environments might not be true, considering the variation of chemical composition in the ISM (e.g., the variation of $\log_{10}(N/O)$ in Croxall et al. 2016). Currently, there is no good observational method to characterize this ratio for all environments. Simulation results suggest that it is reasonable to treat it as a constant at this point (e.g., Ma et al. 2016). (b) We use metallicity gradients instead of a complete metallicity map, which might cause an artificial correlation between the D/M and galactocentric radius. In massive spiral galaxies, the variation of metallicity is dominated by the radial gradient, and the azimuthal scatter is considered second order. Berg et al. (2015) and Croxall et al. (2016) measured a representative azimuthal scatter of ∼0.1 dex in M101 and NGC 628, which is small compared to the radial gradient but nonnegligible. Kreckel et al. (2019) found that the typical scatter of $12 + \log_{10}(O/H)$ at a given radius in the PHANGS-MUSE samples is small, around 0.03–0.05 dex. There are ongoing efforts toward fitting a complete $12 + \log_{10}(O/H)$ map from the sight lines of H I regions (T. Williams et al. 2020, in preparation). Their preliminary results also show that the radial gradient dominates the variation in $12 + \log_{10}(O/H)$.

2.4. SFR and Stellar Mass

We use the GALEX (Martin et al. 2005) and WISE (Wright et al. 2010) maps to trace SFR surface density ($\Sigma_{\rm SFR}$) and stellar mass surface density ($\Sigma_\star$). For both the GALEX and WISE maps, we use the *z*0MGS data products (Leroy et al. 2019) with a resolution of 15″. The correction for the MW extinction in the GALEX maps has been included in the *z*0MGS data products.

The continuum at the GALEX far-UV (FUV) band (∼154 nm) is dominated by the light from relatively young ($\lesssim$100 Myr) stars, so we can estimate $\Sigma_{\rm SFR}$ from the FUV flux ($I_{\rm FUV}$). Since interstellar dust absorbs the starlight and reemits it in the IR (Calzetti et al. 2007; Kennicutt & Evans 2012), we further improve the estimation by correcting the $I_{\rm FUV}$ with local dust extinction using WISE W4 (∼22 μm) flux ($I_{\rm W4}$). We adopt the hybrid SFR calibrations in Table 7 of Leroy et al. (2019):

$$\Sigma_{\rm SFR}\,[M_\odot\,{\rm yr}^{-1}\,{\rm kpc}^{-2}] \approx 8.85\times10^{-2} I_{\rm FUV}\,[{\rm MJy\,sr}^{-1}] + 3.02\times10^{-3} I_{\rm W4}\,[{\rm MJy\,sr}^{-1}]\ . \quad (10)$$

Note that although we adopt GALEX FUV maps that have been corrected for the MW extinction, the IC 342 $\Sigma_{\rm SFR}$ derived from GALEX FUV could be uncertain due to its high MW extinction. However, the impact is small, since the $\Sigma_{\rm SFR}$ is dominated by the WISE W4 term.

We use the WISE W1 (∼3.4 μm) maps to trace $\Sigma_\star$. We adopt a stellar-to-W1 mass-to-light ratio, $\Upsilon_\star^{3.4}$, from *z*0MGS[14] (Leroy et al. 2019). We then use this $\Upsilon_\star^{3.4}$ to calculate $\Sigma_\star$ from WISE W1 flux ($I_{\rm W1}$):

$$\Sigma_\star\,[M_\odot\,{\rm pc}^{-2}] \approx 3.3\times10^2\left(\frac{\Upsilon_\star^{3.4}}{0.5}\right) I_{\rm W1}\,[{\rm MJy\,sr}^{-1}]. \quad (11)$$

[14] Here $\Upsilon_\star^{3.4} = 0.21$, 0.5, 0.29, 0.28, and 0.31 for IC 342, M31, M33, M101, and NGC 628, respectively.

2.5. Ratios and Fractions

We use three derived ratios and fractions in the following analysis, which are calculated with the following formulae:

$$\mathrm{D/M} \equiv \frac{\Sigma_d}{\Sigma_{\rm metal}} = \frac{\Sigma_d}{\Sigma_{\rm gas} \times Z}, \tag{12}$$

$$f_{\rm H_2} \equiv \frac{\Sigma_{\rm mol}}{\Sigma_{\rm gas}}, \tag{13}$$

and

$$f_{\rm gas} \equiv \frac{\Sigma_{\rm gas}}{\Sigma_{\rm gas} + \Sigma_\star}. \tag{14}$$

Note that whenever we calculate the galaxy-averaged or radial-binned values of these quantities, we calculate the ratio of averages, instead of the average of ratios.

2.6. Dynamical Equilibrium Pressure

We use the midplane dynamical equilibrium pressure ($P_{\rm DE}$) to trace the volume density of gas in the ISM. We estimate the $P_{\rm DE}$ with the same basic formulism in Elmegreen (1989), Leroy et al. (2008), Gallagher et al. (2018), and Sun et al. (2020):

$$P_{\rm DE} = \frac{\pi G}{2}\Sigma_{\rm gas}^2 + \Sigma_{\rm gas}\sqrt{2G\rho_\star}\,\sigma_{{\rm gas},z}. \tag{15}$$

The first term represents the weight of the ISM due to the self-gravity of the ISM disk ($P_{\rm DE,self}$). The second term is the weight of the ISM due to stellar gravity ($P_{\rm DE,\star}$). Here $\sigma_{{\rm gas},z}$ is the vertical gas velocity dispersion. We adopt a constant value of $\sigma_{{\rm gas},z} = 11\ {\rm km\ s^{-1}}$ from Leroy et al. (2008). Here $\rho_\star$ is the stellar mass volume density near the midplane. We estimate $\rho_\star$ with

$$\rho_\star = \frac{\Sigma_\star}{4H_\star} = \frac{\Sigma_\star}{0.12R_{25}}, \tag{16}$$

where $H_\star$ is the stellar scale height. We estimate $H_\star$ with a fixed flattening ratio $R_{25}/H_\star = 33.6$ (Leroy et al. 2008; Sun et al. 2020). The systematic uncertainty in $P_{\rm DE}$ resulting from the adopted $\sigma_{{\rm gas},z}$ and the R_{25}-to-$H_\star$ conversion is ∼0.1–0.2 dex (Leroy et al. 2008; Sun et al. 2020). This is not included in the following Monte Carlo analysis because it is not a random error.

3. D/M and the CO-to-H_2 Conversion Factor

In this section, we propose a novel approach to constraining the D/M and $\alpha_{\rm CO}$ simultaneously by examining the resolved environmental dependence of the D/M on metallicity and ISM gas density. We expect that if all relevant quantities are accurately measured, we should observe the D/M increasing or staying constant with both metallicity and ISM gas density. It has been demonstrated in several depletion-based D/M studies that the D/M is positively correlated with both metallicity and gas volume density (Jenkins 2009, 2014; Roman-Duval et al. 2019b; Péroux & Howk 2020). From a theoretical perspective, it is also shown that if dust growth dominates over other dust input mechanisms, the D/M would be positively correlated with both metallicity and ISM gas density; if the dust growth rate is lower due to either low dust or gas-phase metal abundance, the D/M would stay roughly constant (Hirashita 1999; Inoue 2003; Zhukovska et al. 2008; Asano et al. 2013; Rowlands et al. 2014; De Vis et al. 2017; Hou et al. 2019; Aoyama et al. 2020).

We take $12 + \log_{10}({\rm O/H})$ and $P_{\rm DE}$ as tracers for metallicity and ISM gas density, respectively. We calculate the Pearson correlation coefficients of the radial dependence to quantify the D/M–$12 + \log_{10}({\rm O/H})$ and D/M–$P_{\rm DE}$ correlations. In Section 3.1, we first calculate the D/M with four existing $\alpha_{\rm CO}$ prescriptions and examine the D/M–$12 + \log_{10}({\rm O/H})$ and D/M–$P_{\rm DE}$ correlations. In Section 3.2, we attempt to constrain the D/M and $\alpha_{\rm CO}$ simultaneously with the expected correlations. In Section 3.3, we summarize the results in the above two sections. We show the profiles of all measurements calculated with $\alpha_{\rm CO}^{\rm B13}$ in the Appendix.

3.1. Inspecting α_{CO} Prescriptions

We calculate $\Sigma_{\rm gas}$ and D/M with four widely used $\alpha_{\rm CO}$ prescriptions (Section 2.2.2) and examine their resulting D/M–environment relations. In Figure 2, we show the D/M versus $12 + \log_{10}({\rm O/H})$ and $P_{\rm DE}$ calculated from the four $\alpha_{\rm CO}$ prescriptions. The Pearson correlation coefficients of the radial trends within each galaxy are presented in Table 4. The variances of the correlation coefficients are derived with the 16th/84th percentiles from 1000 Monte Carlo tests, assuming Gaussian uncertainties in Σ_d, $\Sigma_\star$, $\Sigma_{\rm atom}$, and $I_{\rm CO}$ and coefficients in the $12 + \log_{10}({\rm O/H})$ gradients.

In Figure 2, we notice that IC 342 deviates from the other galaxies in the D/M–$12 + \log_{10}({\rm O/H})$ trend except for $\alpha_{\rm CO}^{\rm B13}$. We also notice that M31 has large uncertainties in the D/M, mainly due to its uncertainties in the metallicity gradient, which makes its correlation coefficients in Table 4 less meaningful.

If we put IC 342 and M31 aside for a moment, we find that all $\alpha_{\rm CO}$ prescriptions except $\alpha_{\rm CO}^{\rm S12}$ yield reasonable D/M–$12 + \log_{10}({\rm O/H})$ and D/M–$P_{\rm DE}$ correlation coefficients. Meanwhile, the correlation coefficients are sensitive to the choice of $\alpha_{\rm CO}$. The $\alpha_{\rm CO}^{\rm MW}$ yields significant positive or insignificant D/M–$12 + \log_{10}({\rm O/H})$ and D/M–$P_{\rm DE}$ correlations. The $\alpha_{\rm CO}^{\rm S12}$ yields significant negative correlations in M33 and M101 and insignificant correlations in NGC 628. The $\alpha_{\rm CO}^{\rm B13}$ yields significant positive correlations. The $\alpha_{\rm CO}^{\rm H15}$ yields significant positive correlations in M101 and NGC 628 and insignificant correlations in M33.

In IC 342, we observe strong negative correlations with small variances with $\alpha_{\rm CO}^{\rm MW}$, $\alpha_{\rm CO}^{\rm S12}$, and $\alpha_{\rm CO}^{\rm H15}$. The $\alpha_{\rm CO}^{\rm B13}$ yields weaker and less significant negative correlations. Meanwhile, the D/M–$12 + \log_{10}({\rm O/H})$ trend in IC 342 stays within the range among the other galaxies with $\alpha_{\rm CO}^{\rm B13}$ in Figure 2. One possible reason for the distinct behavior of IC 342 is the starburst region in its center, which could affect dust SED fitting and $\alpha_{\rm CO}$ due to its temperature and gas velocity dispersion. Regarding the dust SED fitting in the center, we have a fairly good fit quality ($\chi^2 \lesssim 1$) and a derived dust temperature ($T_d \sim 25$ K) that can be well described by an MBB within $\lambda = 100$–$500\ \mu$m; thus, we trust our derived Σ_d. Among the $\alpha_{\rm CO}$ prescriptions, $\alpha_{\rm CO}^{\rm B13}$ is the only one that considers the decrease of $\alpha_{\rm CO}$ due to gas temperature and dynamics. These effects are modeled by $\Sigma_{\rm Total}$[15]

[15] Bolatto et al. (2013) used $\Sigma_{\rm Total}$ to model the effects from gas temperature and dynamics for two reasons. (i) The temperature and velocity dispersion effects are more important in galaxy centers and ultraluminous infrared galaxies. These regions can be captured by $\Sigma_{\rm Total}$ with a lower bound in general. (ii) The $\Sigma_{\rm Total}$ is more easily measurable than the temperature and velocity dispersion.

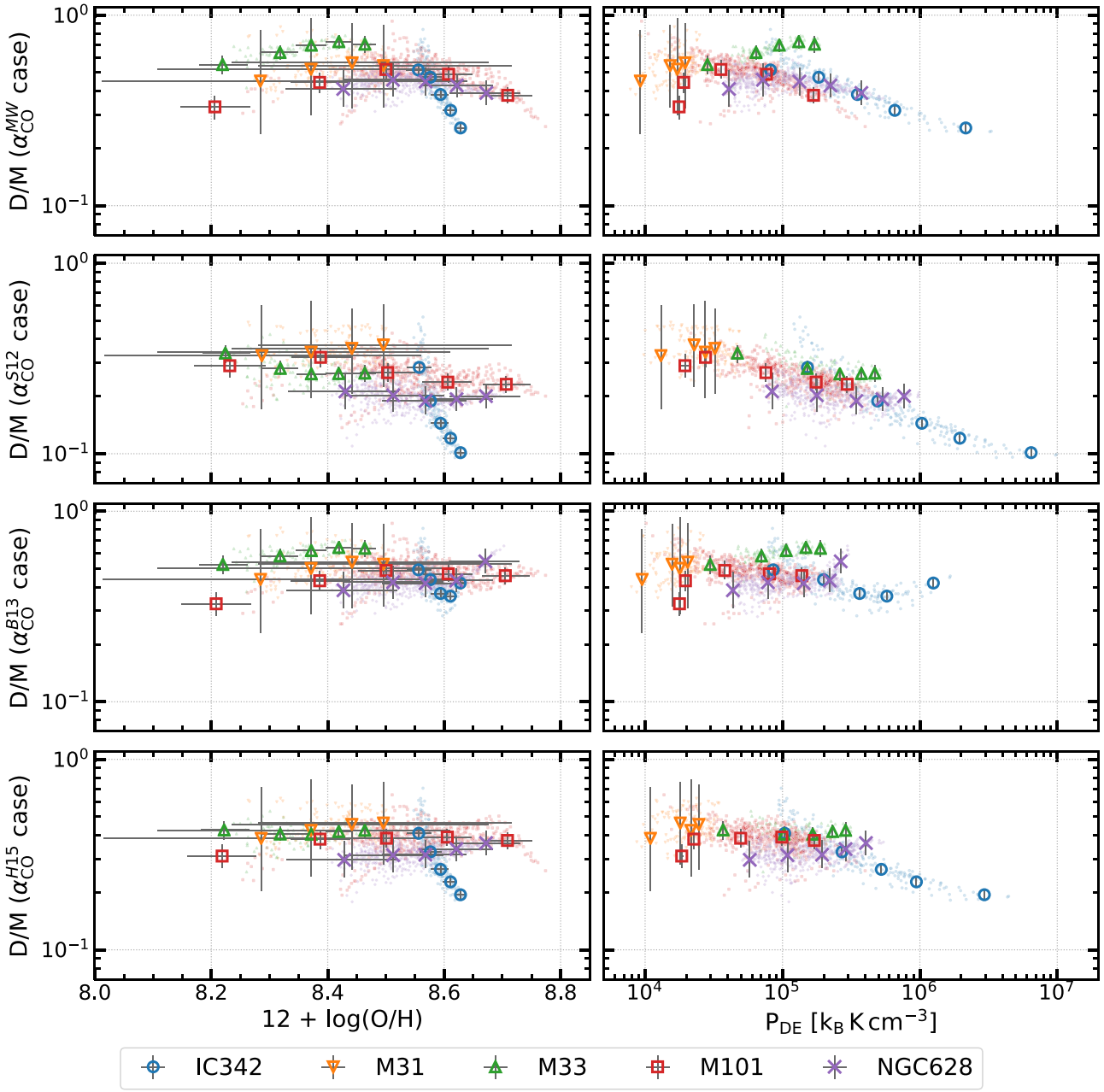

Figure 2. Measured D/M as calculated with four different α_{CO} prescriptions. The large symbols are radial-binned values, while the small, faint symbols are the pixel-by-pixel values where detection is above 3σ. The error bar shows the 16th/84th percentile distribution from 1000 Monte Carlo tests assuming a Gaussian error in the measurements. The x-axes are 12 + $\log_{10}$(O/H) and P_{DE}, which are our tracers for metallicity and gas volume density, respectively.

in Bolatto et al. (2013). This consideration likely results in the least negative D/M–12 + $\log_{10}$(O/H) and D/M–P_{DE} correlation coefficients.

In summary, given that we expect the D/M to increase or stay constant with both 12 + $\log_{10}$(O/H) and P_{DE}, α_{CO}^{B13} seems to give the most reasonable D/M among the four prescriptions across all environments. The D/M calculated with α_{CO}^{B13} has a mean value of 0.46 and a 1σ range spanning 0.40–0.58. The α_{CO}^{MW} and α_{CO}^{H15} yield reasonable correlations in M33, M101, and NGC 628 but result in strong negative correlations in IC 342. Two effects likely contribute to this. One is the distinct behavior of α_{CO} due to the high Σ_{gas} and $\Sigma_{\star}$, which is not considered in α_{CO} prescriptions parameterized by metallicity only, e.g., α_{CO}^{S12} and α_{CO}^{H15}. The other is that, due to the high f_{H_2} in IC 342, the variation of α_{CO} has a larger impact on the D/M, P_{DE}, and their relevant correlations.

3.2. Constraining α_{CO} with D/M–12+log$_{10}$(O/H) and D/M–P$_{DE}$ Relations

We demonstrated that the resolved behavior of the D/M is sensitive to the assumed conversion factor. Here we propose a novel approach to constrain α_{CO} by the expected D/M–metallicity and D/M–ISM gas density behaviors that aims at solving the D/M and α_{CO} simultaneously. In the following, we present a first attempt at using this novel method to study the

Table 4
Pearson Correlation Coefficients of the Radial D/M–12 + $\log_{10}$(O/H) and D/M–P_{DE} Dependence Within Each Galaxy

Galaxy	Quantity	Prescription			
		α_{CO}^{MW}	α_{CO}^{S12}	α_{CO}^{B13}	α_{CO}^{H15}
IC 342	corr(D/M, 12 + $\log_{10}$(O/H))	$-0.99^{+0.02}_{-0.01}$	$-0.99^{+0.01}_{-0.01}$	$-0.65^{+0.23}_{-0.13}$	$-0.99^{+0.01}_{-0.01}$
	corr(D/M, P_{DE})	$-0.89^{+0.01}_{-0.10}$	$-0.78^{+0.01}_{-0.21}$	$-0.31^{+0.01}_{-0.46}$	$-0.83^{+0.01}_{-0.16}$
M31	corr(D/M, 12 + $\log_{10}$(O/H))	$0.90^{+0.09}_{-0.99}$	$0.99^{+0.01}_{-1.79}$	$0.92^{+0.07}_{-1.07}$	$0.98^{+0.01}_{-1.25}$
	corr(D/M, P_{DE})	$0.93^{+0.01}_{-0.36}$	$0.54^{+0.21}_{-1.01}$	$0.91^{+0.02}_{-0.38}$	$0.75^{+0.09}_{-0.49}$
M33	corr(D/M, 12 + $\log_{10}$(O/H))	$0.94^{+0.02}_{-0.28}$	$-0.89^{+0.35}_{-0.05}$	$0.97^{+0.01}_{-0.43}$	$-0.02^{+0.71}_{-0.60}$
	corr(D/M, P_{DE})	$0.86^{+0.11}_{-0.18}$	$-0.81^{+0.17}_{-0.14}$	$0.91^{+0.05}_{-0.34}$	$0.13^{+0.52}_{-0.78}$
M101	corr(D/M, 12 + $\log_{10}$(O/H))	$0.42^{+0.17}_{-0.14}$	$-0.83^{+0.21}_{-0.08}$	$0.82^{+0.07}_{-0.08}$	$0.75^{+0.14}_{-0.20}$
	corr(D/M, P_{DE})	$-0.13^{+0.42}_{-0.01}$	$-0.89^{+0.12}_{-0.08}$	$0.47^{+0.25}_{-0.01}$	$0.40^{+0.34}_{-0.06}$
NGC 628	corr(D/M, 12 + $\log_{10}$(O/H))	$-0.30^{+0.97}_{-0.43}$	$-0.63^{+1.40}_{-0.27}$	$0.85^{+0.09}_{-0.18}$	$0.96^{+0.03}_{-0.29}$
	corr(D/M, P_{DE})	$-0.62^{+1.22}_{-0.17}$	$-0.46^{+1.18}_{-0.47}$	$0.84^{+0.05}_{-0.26}$	$0.98^{+0.01}_{-0.35}$

Note. The upper and lower variances are quoted from the 16th and 84th percentiles of 1000 Monte Carlo tests (see text).

parameter space for the widely used simple metallicity power-law prescriptions for α_{CO}.

We model α_{CO} as a simple power law parameterized with metallicity, that is,

$$\log_{10}\frac{\alpha_{CO}}{1\ M_{\odot}\ \mathrm{pc}^{-2}\ (\mathrm{K\ km\ s}^{-1})^{-1}} = a + b \times (12 + \log_{10}(\mathrm{O/H}) - 8.69). \quad (17)$$

We then constrain the parameter space [a, b] to only include the nonnegative D/M–12 + $\log_{10}$(O/H) and D/M–P_{DE} correlations. We further constrain the parameter space with D/M < 1 to ensure the sanity of the resulting prescription. Practically, we relax the lower bound of the correlation coefficient to $\rho > -0.1$ to compensate for uncertainties in measurements. For the same reason, we relax the maximum D/M to 1.2.

We explore the parameter space $0.0 \leqslant a \leqslant 1.25$, which is equivalent to a normalization of $0.25 \leqslant \alpha_{CO}/\alpha_{CO}^{MW} \leqslant 4.0$ at solar metallicity. The range of b is $-4 \leqslant b \leqslant 0.5$, which generously encompasses the slopes from previous extragalactic studies, which typically find $\alpha_{CO} \propto Z^{-1}$ to Z^{-3} (Bolatto et al. 2013).

The constraints are visualized in the power-law parameter space in Figure 3. In the "allowed space" column, we see the maximum D/M constraints on the minimum normalization so that the resulting α_{CO} does not yield an unphysical D/M in galaxy centers. The D/M–12 + $\log_{10}$(O/H) and D/M–P_{DE} correlations constrain the maximum normalization at a fixed slope. They limit the upper bound of Σ_{gas}, and thus the lower bound of the D/M, in galaxy centers, so the α_{CO} does not yield negative correlations. The boundaries drawn by the two correlation constraints are similar to each other, while the constraint set by the D/M–P_{DE} correlation is usually more strict than the D/M–12 + $\log_{10}$(O/H) correlation constraint.

Among the galaxies, IC 342 has the narrowest allowed space, which primarily defines the parameter space allowed in all galaxies. The median D/M in this allowed space is high within IC 342 and across all galaxies, implying that this space satisfies all constraints by minimizing Σ_{gas} and creating a high, flat D/M. In M31, all constraints are easily satisfied within the parameter space we explore. In the allowed parameter space, M33, M101, and NGC 628 have a large overlapping region. The D/M upper limit constraint in M101 marks part of the boundary of the parameter space allowed in all galaxies.

We overlay four power-law or power-law-like α_{CO} prescriptions, i.e., α_{CO}^{MW}, α_{CO}^{S12}, α_{CO}^{H15}, and the Accurso et al. (2017) prescription, on the parameter space. For α_{CO}^{H15}, we only plot its low-metallicity solution. The complete α_{CO}^{H15} formula would be the space between α_{CO}^{MW} and α_{CO}^{H15} in Figure 3. We show Accurso et al. (2017) because it is a widely used power-law α_{CO}. We did not include it in the previous analysis because it yields results similar to α_{CO}^{S12}. To fit Accurso et al. (2017) into the two-dimensional space, we assume $\Delta MS = 0$ in their Equation (25). In M33, M101, and NGC 628, these prescriptions sit near the boundary of the correlation constraints. In IC 342, these prescriptions are far from the allowed space.

The space that satisfies all constraints in all galaxies (bottom left panel in Figure 3) has a small normalization and flat slope. The normalization spans $0.2 \lesssim \alpha_{CO}/\alpha_{CO}^{MW} \lesssim 0.3$ at solar metallicity, and the slope spans $-1 \lesssim b \lesssim 0.5$. Although we do find a parameter space where all constraints are satisfied, it is almost solely defined by IC 342. We do not proceed with the D/M analysis with this parameter space, as it yields a median D/M that seems too high compared to depletion observations.

The results from this test demonstrate that in galaxies except IC 342, a simple power-law α_{CO} parameterized with metallicity can yield expected physics. Among the tested existing α_{CO} prescriptions, α_{CO}^{MW}, α_{CO}^{H15}, and Accurso et al. (2017) satisfy most constraints in galaxies except IC 342, while α_{CO}^{S12} seems to have a normalization that is too high (2 α_{CO}^{MW} at $Z_{\odot}$). When we include IC 342, the only space that satisfies all constraints yields a D/M that seems too high, and the tested existing α_{CO} prescriptions are far outside this allowed space. This suggests that one would probably need a more sophisticated functional form to properly model α_{CO} across all environments (e.g., the starburst region in IC 342). One example is the Bolatto et al. (2013) prescription, where the authors attempt to model the decrease of α_{CO} in the high-Σ_{Total} regions due to the combined effects of gas temperature and velocity dispersion.

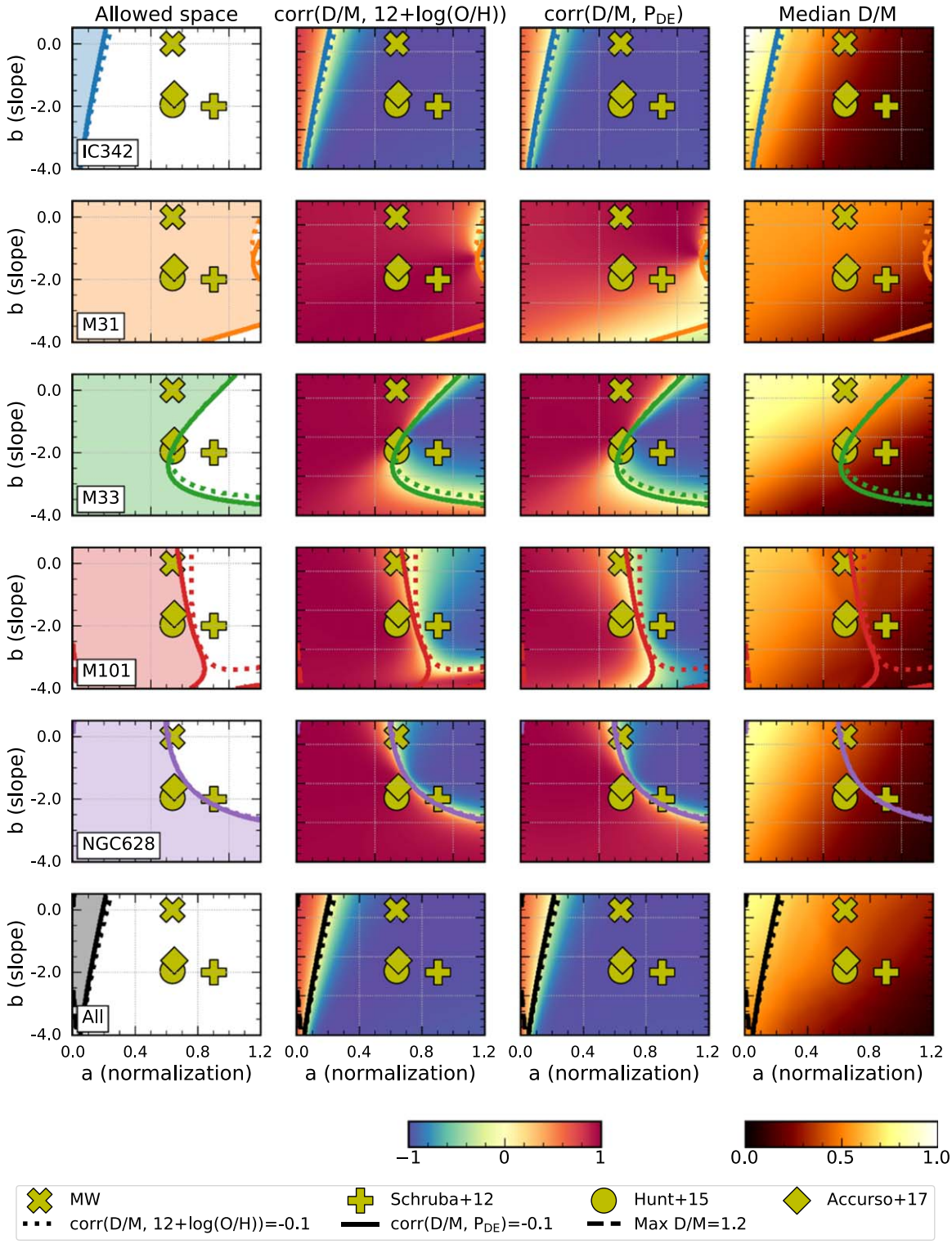

Figure 3. Power-law parameter space with the three constraints in each galaxy. In the "allowed space" column, the shaded area shows the region where all three constraints are satisfied. The cross, plus sign, circle, and diamond mark the locations of α_{CO}^{MW}, α_{CO}^{S12}, α_{CO}^{H15}, and the Accurso et al. (2017) α_{CO} in the parameter space, respectively. The dotted, solid, and dashed lines show the boundaries of the D/M–12 + $\log_{10}$(O/H) correlation, D/M–P_{DE} correlation, and D/M upper limit constraints, respectively. In the middle two columns, the color map shows the Pearson correlation coefficients. In the "median D/M" column, the color map shows the pixel-by-pixel median D/M. To fit the two-dimensional space, we assume $Z < Z_{\odot}$ for α_{CO}^{H15} and $\Delta MS = 0$ for the Accurso et al. (2017) prescription. All α_{CO} prescriptions shown here locate outside the space satisfying all constraints, which implies that extra parameters are needed in α_{CO} modeling to obtain a reasonable D/M across physical environments.

3.3. Section Summary

We showed that the D/M is sensitive to the choice of α_{CO}. Among the prescriptions in Section 3.1, α_{CO}^{B13} gives the most reasonable D/M. This is inferred from the D/M–12 + $\log_{10}$(O/H) and D/M–P_{DE} correlations, especially in IC 342. In Section 3.2, we use a new approach to constrain the D/M and α_{CO} simultaneously. However, in this first attempt, we show that the

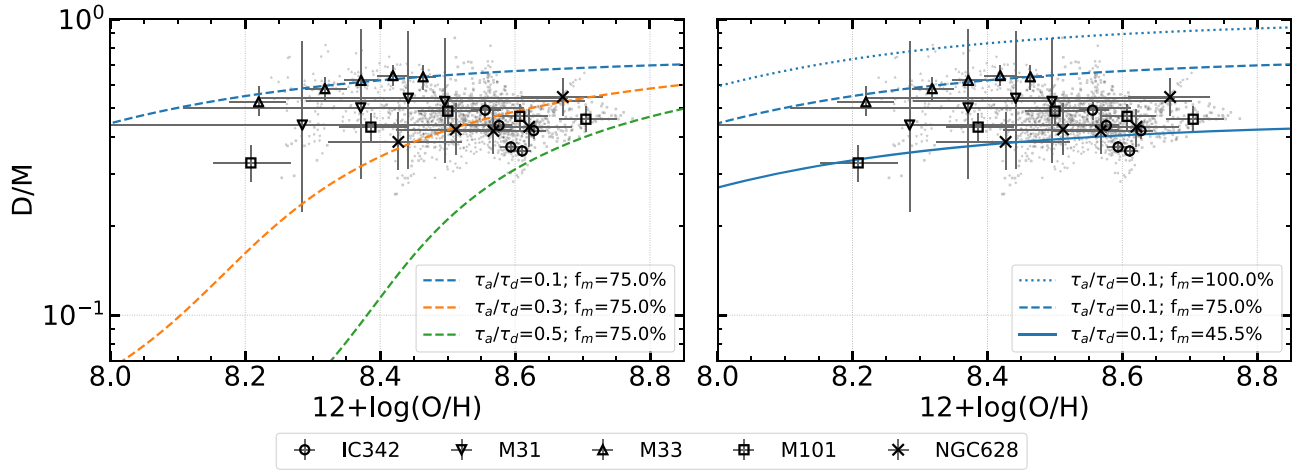

Figure 4. Our measurements and the Aniano et al. (2020) dust evolution model. Left: fixing f_m and varying τ_a/τ_d, showing that the variation of the D/M is smaller with lower τ_a/τ_d. Right: fixing τ_a/τ_d and varying f_m, showing that larger f_m results in a higher D/M. Black symbols: this work. Each symbol corresponds to a galaxy, as shown in the legend.

$\alpha_{\rm CO}$ satisfying all constraints yields a D/M that is too high compared to depletion observations. Thus, we proceed with the $\alpha_{\rm CO}^{\rm B13}$ case for the following analysis.

The median and 16th/84th percentile of our observed D/M calculated with $\alpha_{\rm CO}^{\rm B13}$ is $0.46^{+0.12}_{-0.06}$. This is consistent with the values adopted in Clark et al. (2016, 2019), which are 0.5 ± 0.1 and 0.4 ± 0.2, respectively. The median D/M and the 16th/84th percentile in each galaxy are $0.41^{+0.11}_{-0.05}$, $0.50^{+0.11}_{-0.06}$, $0.60^{+0.05}_{-0.06}$, $0.48^{+0.06}_{-0.05}$, and $0.43^{+0.03}_{-0.04}$ for IC 342, M31, M33, M101, and NGC 628, respectively. Due to our limited understanding of the CO-to-H_2 conversion factor, we cannot conclusively determine the environmental dependence of the D/M. We present the observed environmental dependence calculated with $\alpha_{\rm CO}^{\rm B13}$ in the Appendix.

4. Discussion

4.1. Implications of the Observed D/M

In Section 3, we calculate the D/M with several common $\alpha_{\rm CO}$ prescriptions and the parameter space of a power-law $\alpha_{\rm CO}$ parameterized by metallicity. Although we have not fully explored all possible descriptions of $\alpha_{\rm CO}$, we proceed with the analysis with the most reasonable prescription, $\alpha_{\rm CO}^{\rm B13}$, at the moment. The $\alpha_{\rm CO}^{\rm B13}$ yields a fairly constant D/M over a wide range of physical environments, with a median D/M = 0.46. From dust evolution simulations (Dwek 1998; Asano et al. 2013; Aoyama et al. 2020), one possible explanation for a constant D/M is that dust growth dominates the increase of the D/M, and the dust growth rate slows down as the available dust-forming metals in the gas phase decrease. Thus, the D/M would stay roughly constant when most dust-forming metals are already locked in dust grains.

This idea can be demonstrated with the toy model in Aniano et al. (2020), which considers dust growth in the ISM, dust injection from AGB stars and SNe, and dust destruction. It is assumed that the effective dust growth timescale (τ_a) is much smaller than the dust injection timescale ($\tau_\star$); thus, this model only applies to ISM environments where dust formation is dominated by dust growth in the ISM. With a quasi-steady-state assumption, the model gives the D/M as a function of metallicity,

$$\mathrm{D/M} = 0.5\frac{f_m}{Z'}\left\{\left(Z' - \frac{\tau_a}{\tau_d}\right) + \left[\left(Z' - \frac{\tau_a}{\tau_d}\right)^2 + 4\frac{\tau_a}{\tau_\star}Z'\right]^{1/2}\right\}, \quad (18)$$

where τ_d is the effective dust destruction timescale, and Z' is the metallicity relative to the solar value. Again, we use $12 + \log_{10}(\mathrm{O/H})_\odot = 8.69$[16]; f_m is the mass fraction of dust-forming metals to the mass of total metals, that is,

$$f_m = \frac{\text{Mass of dust} - \text{forming metals}}{\text{Mass of total metals}}. \quad (19)$$

In Aniano et al. (2020), f_m is fixed at $\sim$45.5%. The dust injection timescale has a minor impact on the prediction. We fix $\tau_a/\tau_\star = 10^{-2}$ throughout all models, since we expect $\tau_a \sim \mathcal{O}(10^7)$ and $\tau_\star \sim \mathcal{O}(10^9)$ yr in the nearby spiral galaxies, e.g., discussions in Draine (2009) and Asano et al. (2013). Note that we do not expect our measurements to follow a single parameter set because the variation in gas density and SFR will reflect on the change in τ_a/τ_d (Asano et al. 2013; Aniano et al. 2020).

We overlay our observed D/M with the model predictions in Figure 4. All of the models predict a higher D/M at higher $12 + \log_{10}(\mathrm{O/H})$, and the D/M asymptotically approaches f_m toward high $12 + \log_{10}(\mathrm{O/H})$. In the left panel, we fix $f_m = 75\%$ and plot three different τ_a/τ_d ratios: 0.1, 0.3, and 0.5. As dust growth becomes faster relative to dust destruction (τ_a/τ_d decreases), the model predicts a smaller variance in D/M in our observed $12 + \log_{10}(\mathrm{O/H})$ range. In other words, with a lower τ_a/τ_d, the D/M approaches f_m at a smaller $12 + \log_{10}(\mathrm{O/H})$.

In the right panel of Figure 4, we fix τ_a/τ_d at 0.1 and vary f_m. The major parts of our measurements have a D/M above the $f_m = 45.5\%$ model, which means that the fraction of

[16] Note that Aniano et al. (2020) used $12 + \log_{10}(\mathrm{O/H})_\odot = 8.75$.

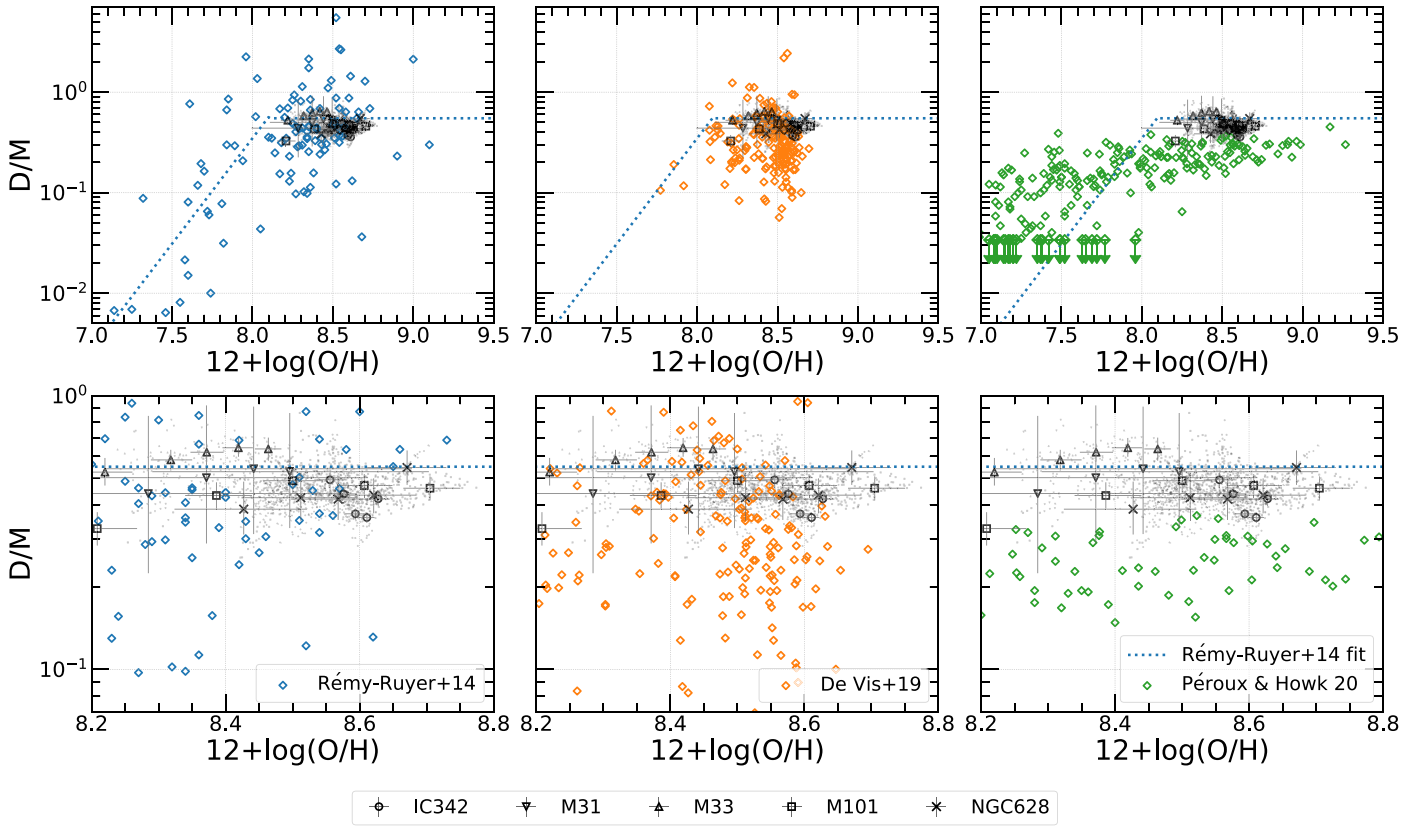

Figure 5. The D/M measured in this work overlaid with previous observations. Data points with arrows show the upper limit. Dotted line: broken power-law fit from Rémy-Ruyer et al. (2014, Table 1). Black symbols: this work. Each symbol corresponds to a galaxy, as shown in the legend. The bottom panels are a zoom-in of the top panels. Left: Rémy-Ruyer et al. (2014) observations ($X_{\rm CO,Z}$ case). Middle: De Vis et al. (2019) observations (PG16S calibration). Right: Péroux & Howk (2020) observations. Our measurements are consistent with Rémy-Ruyer et al. (2014) and De Vis et al. (2019), while the Péroux & Howk (2020) measurements are systematically lower than ours.

dust-forming metals is probably higher than the value estimated in Aniano et al. (2020). For IC 342, M31, M101, and NGC 628, most measured D/M values are between the $f_m = 45.5\%$ and 75% models. This could indicate that the fraction of dust-forming metals is lower than 75% in these galaxies. The galaxy M33 has the overall highest D/M. Within the frame of this model, it can indicate that the chemical composition of the ISM or dust is different in M33 or that τ_a/τ_d in M33 is smaller than in the other galaxies. We will discuss this more in Section 4.3.

4.2. Previous Multigalaxy Observations of D/M

In this section, we compare our measured D/M to previous multigalaxy D/M observations, including both IR- and abundance-based measurements. Further, we inspect whether there are significant differences in the D/M–metallicity relations between the resolved and galaxy-integrated measurements.

Rémy-Ruyer et al. (2014) and De Vis et al. (2019) are two IR-based galaxy-integrated studies in the nearby universe. With a sample size >100 galaxies, both works are the benchmarks of our current understanding of the galaxy-integrated dust properties in the nearby universe. Péroux & Howk (2020) derived the D/M from an elemental abundance ratio with the dust-correction model (De Cia et al. 2016, 2018) in $\gtrsim$200 damped Lyα systems. Their samples have redshifts in the range $0.1 \lesssim z \lesssim 5$, providing us a point of view with different sample selection and methodology. We quote the Rémy-Ruyer et al. (2014) data points from their Table A.1, De Vis et al. (2019) had their data public on their website,[17] and Péroux & Howk (2020) included the data table as one of their supplement materials.

Since De Vis et al. (2019) adopted a different definition of D/M from ours, we show the comparison with both definitions. In this work, we assume that the depletion in H I regions, where we get the $12 + \log_{10}({\rm O/H})$ measurements, is negligible ($\lesssim$0.1 dex; e.g., Peimbert & Peimbert 2010). On the other hand, De Vis et al. (2019) assumed that the $12 + \log_{10}({\rm O/H})$ measured in H I regions only traces gas-phase metals; thus, one needs to consider the mass locked in dust grains to get the total metal mass,[18] that is,

$$({\rm D/M})_{D19} \equiv \frac{\Sigma_d}{\Sigma_d + \Sigma_{\rm metal}}. \quad (20)$$

We show the D/M derived with our definition in Figure 5 and the De Vis et al. (2019) definition in Figure 6. Note that the Péroux & Howk (2020) measurements are not converted in either figure due to their D/M-derivation methodology. Péroux & Howk (2020) derived the D/M with a dust-corrected model (De Cia et al. 2016, 2018), which already includes both the gas-phase metal and metal in dust.

[17] http://dustpedia.astro.noa.gr/

[18] In an environment with D/M $\sim$ 0.5 in our definition, the "dust correction" to metallicity under the De Vis et al. (2019) definition is effectively $\sim$+0.18 dex, which seems to be overestimating the available metals compared to the estimated depletion in H I regions.

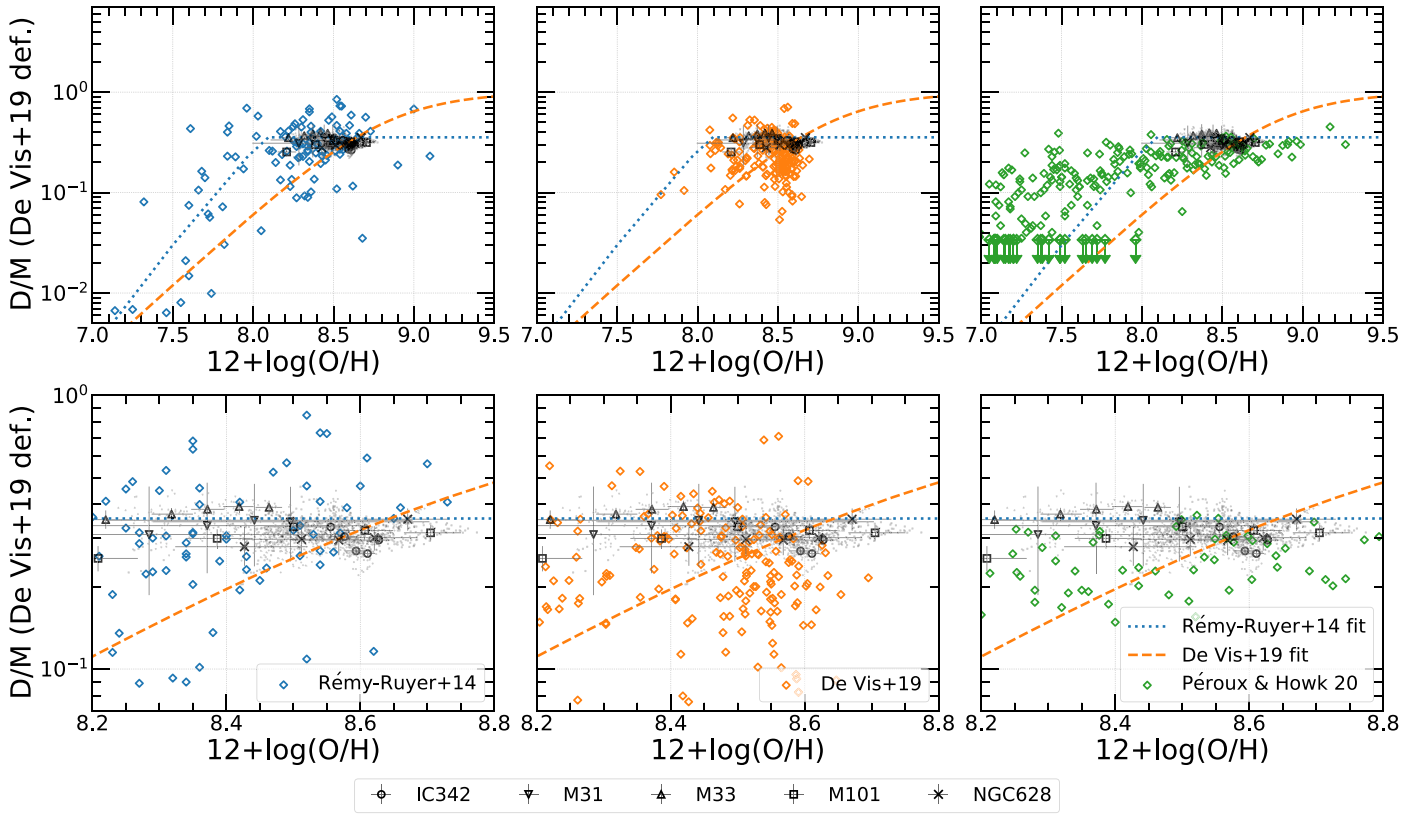

Figure 6. Same as Figure 5 but plotted with the D/M definition in De Vis et al. (2019; except the Péroux & Howk 2020 data; see main text). Orange dashed line: De Vis et al. (2019) D/G–12 + $\log_{10}$(O/H) fit, converted to D/M–12 + $\log_{10}$(O/H) space.

In Figures 5 and 6, we show the Rémy-Ruyer et al. (2014) measurements in the left panels and their fit (the gas-to-dust ratio fit with a broken power law converted to the D/M-to-12 + $\log_{10}$(O/H) $X_{CO,Z}$ case) in all panels. Our measurements locate roughly in the center of their measurements at the same metallicity, and our measurements are also consistent with their broken power law at the high-metallicity end. Both facts suggest that our D/M-to-metallicity relations are consistent with the Rémy-Ruyer et al. (2014) measurements. Note that in the high-metallicity region, the Rémy-Ruyer et al. (2014) broken power law gives a constant D/M, which matches our measurements that the D/M is roughly a constant across galaxies. In Figure 5, there are some Rémy-Ruyer et al. (2014) measurements with D/M > 1. Since their adopted α_{CO} (Schruba et al. 2012) has relatively large normalization (see Figure 2), those high D/M values are not likely due to underestimating Σ_{gas} from the choice of α_{CO}. Instead, it is more likely an issue in the adopted dust opacity function, differences in dust SED fitting techniques, or differences in metallicity calibration.

In the middle panels of Figures 5 and 6, we present the De Vis et al. (2019) measurements (PG16S calibration) and ours. We only select data points where both H I and H_2 measurements are available in De Vis et al. (2019). We also convert their D/G–12 + $\log_{10}$(O/H) fit to D/M–12 + $\log_{10}$(O/H) and plot it in all panels in Figure 6. Note that this fit is not created for the purpose of predicting D/M; thus, it is possible to generate an unphysical D/M at high metallicity due to its power-law nature in our definition of D/M. Our measured D/M scatters around the upper end of the De Vis et al. (2019) data range in both figures.

We present the Péroux & Howk (2020) measurements in the right panels of Figures 5 and 6. Péroux & Howk (2020) derived their D/M by converting observed elemental abundance ratios into depletion with the empirical formulae in De Cia et al. (2016, 2018). They show that as metallicity increases, D/M increases and the scatter of D/M decreases. This trend is shown over all redshifts. In Figure 5, our measured D/M is systematically higher than the D/M in Péroux & Howk (2020). There are two possible causes for the offset. First, the sample selection in Péroux & Howk (2020) is based on H I column density, and a lot of the data come from H I-dominated regions, while most of our data points are in H_2-dominated regions. In other words, the offset might come from the difference in dust evolution in H I- and H_2-dominated regions. Second, there might be a systematic offset between the IR- and abundance-based D/M determination.

4.3. The High D/M in M33

In our measurements, we find that M33 has a higher D/M than the other galaxies at the same metallicity. One possibility is that the α_{CO} in M33 is larger than α_{CO}^{B13}. Gratier et al. (2010) and Druard et al. (2014) suggested a constant $\alpha_{CO} = 2\alpha_{CO}^{MW}$, which is larger than α_{CO}^{B13} everywhere in M33. If we use $2\alpha_{CO}^{MW}$ for M33, the median D/M in M33 will slightly decrease from 0.60 to 0.56, which brings it closer to the other galaxies.

On the other hand, we could also try to interpret this higher D/M with the Aniano et al. (2020) dust evolution model. The first possibility is that f_m is higher in M33. That means the ISM chemical composition is different in M33, and there is a larger fraction of dust-forming metals or a higher ratio of

dust-forming metals to oxygen abundance. The second possibility is a shorter τ_a or longer τ_d in M33. This explanation is less likely because M33 does not seem to have a higher $P_{\rm DE}$ or $\Sigma_{\rm SFR}$ relative to the other galaxies, which are the two key factors affecting τ_a and τ_d.

4.4. Future Perspectives in α_{CO} Constraints

In Section 3.1, we show that the D/M is sensitive to the choice of $\alpha_{\rm CO}$. We find the most reasonable D/M with $\alpha_{\rm CO}^{\rm B13}$; however, we still have negative D/M–metallicity and D/M–density correlations, especially in IC 342. In Section 3.2, we demonstrate that a $\alpha_{\rm CO}$ prescription described by a simple power law with metallicity is not enough to solve the negative correlations. We need a more complex functional form or to take the effects from other environmental parameters, e.g., gas temperature or velocity dispersion, into account. Unfortunately, we do not have enough data points with high $\Sigma_{\rm Total}$, and the fitting results are currently biased toward the center of IC 342 if we adopt the Bolatto et al. (2013) functional form with our constraints.

To continue investigating the effect of $\Sigma_{\rm Total}$, one needs to study nearby galaxies with high-resolution $\Sigma_{\rm gas}$ data, e.g., the PHANGS (A. K. Leroy et al. 2020, in preparation) galaxies. Meanwhile, the analysis is also limited by the resolution of dust maps and FIR observations. Among the existing and retired FIR telescopes, Herschel has the highest spatial resolution, $\sim$1.8 kpc at a distance of 10 Mpc. The resolution is not enough if we want to resolve a $<$1 kpc high surface density region. A future mission of FIR photometry at higher resolution is needed to improve our understanding of ISM dust.

Meanwhile, the Bolatto et al. (2013) functional form is less applicable to distant galaxies because it is built on resolved measurements of $\Sigma_{\rm gas}$ and $\Sigma_\star$. One possible approach to apply the $\alpha_{\rm CO}^{\rm B13}$ prescription to distant galaxies is to derive a conversion from galaxy-integrated quantities to total molecular gas mass derived with $\alpha_{\rm CO}^{\rm B13}$ in resolved galaxies. A larger sample of galaxies with CO emission, stellar mass, and resolved metallicity measurements is required for this approach. Auxiliary data like SFR and total atomic gas mass might also be helpful in the derivation.

5. Summary

We investigate the relation between the D/M and various local ISM environmental quantities in five nearby galaxies: IC 342, M31, M33, M101, and NGC 628. The multiwavelength data from both archival and new observations are processed uniformly. An MBB model with a broken power-law emissivity is used to model the dust emission SED, together with the fitting techniques and dust opacity calibration proposed by Gordon et al. (2014) and implemented in Chiang et al. (2018; Section 2.1). We utilize metallicity gradients derived from auroral line measurements in H I regions to ensure a uniform and high-quality metallicity determination wherever possible. We calibrate and image a new IC 342 H I 21 cm map from new VLA observations. This is part of the observations in the Every-THINGS project (PI: K. M. Sandstrom; I. Chiang et al. 2020, in preparation). All maps are convolved to a common physical resolution at $\sim$2 kpc for a uniform analysis.

We propose a new approach to constrain the D/M and the CO-to-H_2 conversion factors ($\alpha_{\rm CO}$); that is, we use the expected D/M–metallicity and D/M–ISM gas density correlations measured by depletion studies to evaluate the results. We use this conceptual approach to examine the D/M yielded by existing $\alpha_{\rm CO}$ prescriptions and demonstrate our first attempt at utilizing this approach to constrain a simple metallicity power-law $\alpha_{\rm CO}$. We find the following key points.

1. Among the prescriptions we test, $\alpha_{\rm CO}^{\rm B13}$ yields the most reasonable D/M.
2. With $\alpha_{\rm CO}^{\rm B13}$, the D/M is roughly a constant $(0.46^{+0.12}_{-0.06})$ across a large range of ISM environments.
3. When we exclude IC 342, $\alpha_{\rm CO}^{\rm MW}$ and $\alpha_{\rm CO}^{\rm H15}$ can satisfy most constraints set by the D/M–metallicity and D/M–$P_{\rm DE}$ correlations, while $\alpha_{\rm CO}^{\rm S12}$ seems to have a normalization that is too high ($2\alpha_{\rm CO}^{\rm MW}$ at $Z_\odot$).
4. The most obvious difference between $\alpha_{\rm CO}^{\rm B13}$ and other prescriptions is the dependence on the total surface density ($\Sigma_{\rm Total} = \Sigma_{\rm gas} + \Sigma_\star$), which decreases $\alpha_{\rm CO}$ in the regions with $\Sigma_{\rm Total} > 100\,M_\odot\,{\rm pc}^{-2}$. This is mostly important in the centers of galaxies and likely starburst regions.
5. To properly account for the H_2 gas in IC 342, it seems that an $\alpha_{\rm CO}$ prescription parameterized by $12 + \log_{10}({\rm O/H})$ only is not enough. The $\alpha_{\rm CO}^{\rm B13}$, which depends on $\Sigma_{\rm Total}$, yields the most reasonable D/M in IC 342.
6. New FIR observations with spatial resolution better than Herschel are needed for investigating the D/M and $\alpha_{\rm CO}$ at high surface density regions.

In Section 4, we interpret our observations with the dust evolution model from Aniano et al. (2020). We also compare our results to the previous galaxy-integrated D/M measurements. We find the following implications regarding our results.

1. The roughly constant D/M implies a shorter dust growth timescale (τ_a) relative to the dust destruction timescale (τ_d).
2. Most of our measurements fall in the range between $f_m = 45.5\%$ and 75%, with f_m being the mass fraction of dust-forming metals.
3. Our measured D/M is consistent with previous IR-based, galaxy-integrated measurements in the nearby universe (Rémy-Ruyer et al. 2014; De Vis et al. 2019).
4. However, our results are systematically higher than the D/M measured in the abundance-based measurements by Péroux & Howk (2020). This could indicate a systematic offset between IR- and abundance-based methods.

Our results demonstrate that the D/M is sensitive to the choice of $\alpha_{\rm CO}$. The $\alpha_{\rm CO}^{\rm B13}$ is our current best choice of $\alpha_{\rm CO}$, which models the decrease of $\alpha_{\rm CO}$ due to gas temperature and velocity dispersion. Our results show a roughly constant D/M across ISM environments. Further investigation is needed to constrain the D/M and $\alpha_{\rm CO}$ simultaneously.

We thank the referee for thoughtful comments that improved the paper. We gratefully acknowledge the hard work of the CHAOS, DustPedia, EDD, HERACLES, HerM33s, MaNGA, PHANGS, THINGS, and z0MGS teams and thank them for making their data publicly available.

I.C. thanks C. R. Choban, H. Hirashita, C. Howk, D. Kereš, and S. Zhukovska for useful discussions about this work. The work of K.S., I.C., A.K.L., D.U., and J.C. is supported by National Science Foundation grant No. 1615728 and NASA ADAP grants NNX16AF48G and NNX17AF39G. The work of A.K.L. and D.U. is partially supported by the National Science

Foundation under grant Nos. 1615105, 1615109, and 1653300. K.K. gratefully acknowledges funding from the Deutsche Forschungsgemeinschaft (DFG; German Research Foundation) in the form of the Emmy Noether Research Group (grant No. KR4598/2-1). T.G.W. acknowledges funding from the European Research Council (ERC) under the European Unions Horizon 2020 research and innovation program (grant agreement No. 694343). J.P. and C.H. acknowledge support from the Programme National "Physique et Chimie du Milieu Interstellaire" (PCMI) of CNRS/INSU with INC/INP, cofunded by the CEA and CNES.

This work uses observations made with the ESA Herschel Space Observatory. Herschel is an ESA space observatory with science instruments provided by European-led Principal Investigator consortia and with important participation from NASA. The Herschel spacecraft was designed, built, tested, and launched under a contract to ESA managed by the Herschel/Planck Project team by an industrial consortium under the overall responsibility of the prime contractor, Thales Alenia Space (Cannes), and including Astrium (Friedrichshafen), responsible for the payload module and system testing at spacecraft level; Thales Alenia Space (Turin), responsible for the service module; and Astrium (Toulouse), responsible for the telescope, with in excess of 100 subcontractors.

The National Radio Astronomy Observatory is a facility of the National Science Foundation operated under cooperative agreement by Associated Universities, Inc. This research is based on observations made with the Galaxy Evolution Explorer (GALEX), obtained from the MAST data archive at the Space Telescope Science Institute, which is operated by the Association of Universities for Research in Astronomy, Inc., under NASA contract NAS 526555. This work is based on observations carried out with the IRAM NOEMA Interferometer and 30 m telescope. IRAM is supported by the INSU/CNRS (France), MPG (Germany), and IGN (Spain). This publication makes use of data products from the Wide-field Infrared Survey Explorer, which is a joint project of the University of California, Los Angeles, and the Jet Propulsion Laboratory/California Institute of Technology, funded by the National Aeronautics and Space Administration. The WSRT is operated by ASTRON (Netherlands Foundation for Research in Astronomy) with support from the Netherlands Foundation for Scientific Research (NWO).

This research made use of Astropy,[19] a community-developed core Python package for astronomy (Astropy Collaboration et al. 2013, 2018). This research has made use of NASA's Astrophysics Data System Bibliographic Services. We acknowledge the usage of the HyperLeda database (http://leda.univ-lyon1.fr). This research has made use of the NASA/IPAC Extragalactic Database (NED), which is funded by the National Aeronautics and Space Administration and operated by the California Institute of Technology.

Facilities: GALEX, Herschel, IRAM:30 m, IRAM: NOEMA, VLA, WISE, WSRT.

Software: Astropy (Astropy Collaboration et al. 2013, 2018), CASA (McMullin et al. 2007), GILDAS,[20] Matplotlib (Hunter 2007), NumPy and SciPy (van der Walt et al. 2011), pandas (McKinney 2010), SAOImage DS9 (Joye et al. 2003).

Appendix
Measurements with $\alpha_{\rm CO}^{\rm B13}$

As we state in Section 3.3, due to our limited understanding of the CO-to-H_2 conversion factor, we do not intend to conclusively determine the environmental dependence of the D/M with the current measurements. However, it is still informative to show our measurements with $\alpha_{\rm CO}^{\rm B13}$ here. We present the radial profiles of the measured and derived quantities in Figure 7. The D/M is roughly constant as the radius increases. On the other hand, most measured quantities decrease as the radius increases, except $f_{\rm gas}$, which increases with radius.

Figure 8 shows the relationship between the physical quantities and the D/M. Generally speaking, the D/M is roughly constant across most physical environments. We also notice that the D/M tends to decrease as $f_{\rm gas}$ increases, which is a similar trend found in the galaxy-integrated measurements in De Vis et al. (2019).

[19] http://www.astropy.org
[20] http://www.iram.fr/IRAMFR/GILDAS

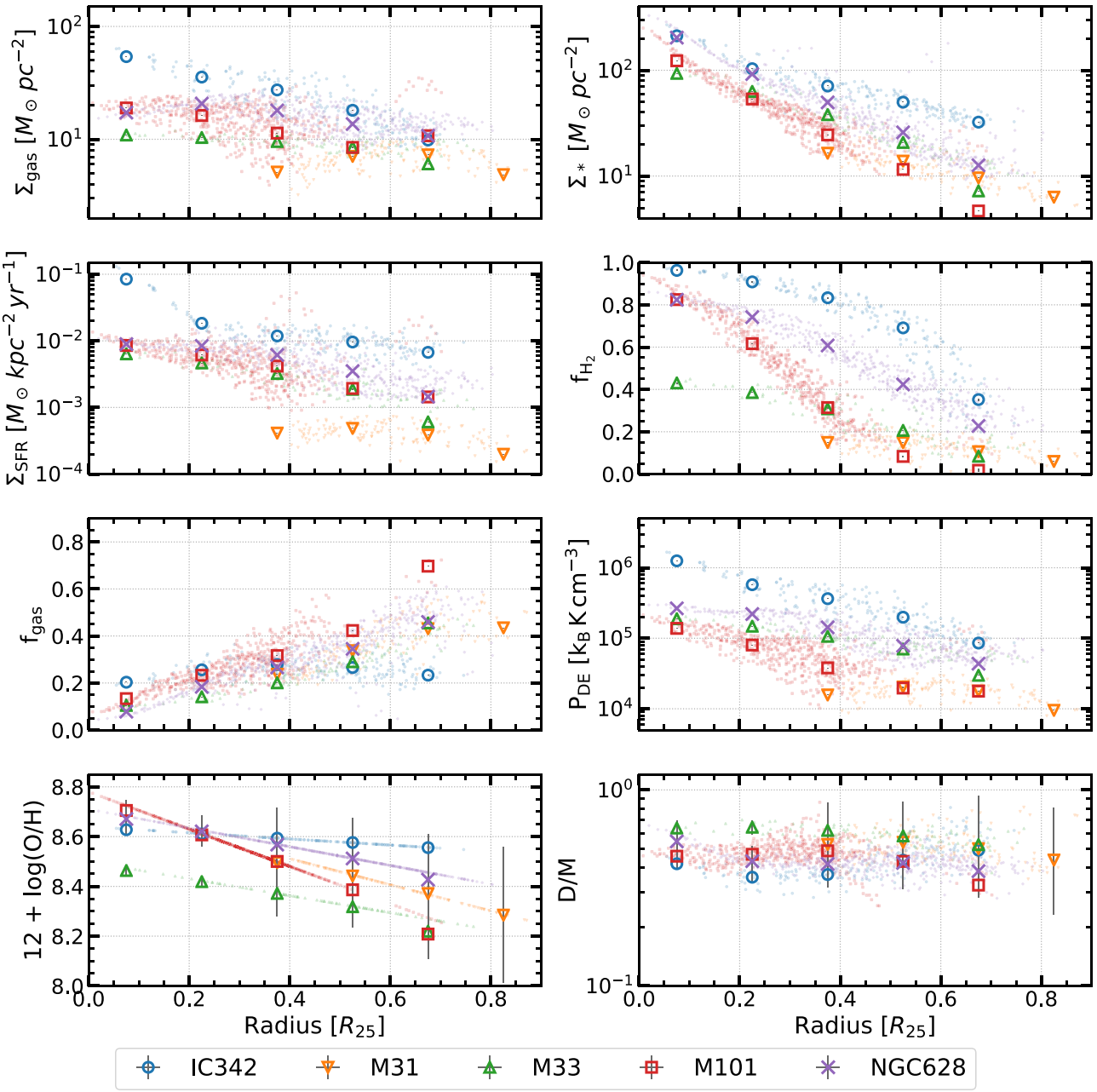

Figure 7. Radial profiles of the observed and derived quantities calculated with α_{CO}^{B13}. Small symbols: pixel-by-pixel data where detection is above 3σ. Large symbols: average in radial bins. The error bar shows the 16th/84th percentile distribution from 1000 Monte Carlo tests, assuming a Gaussian error in the measurements.

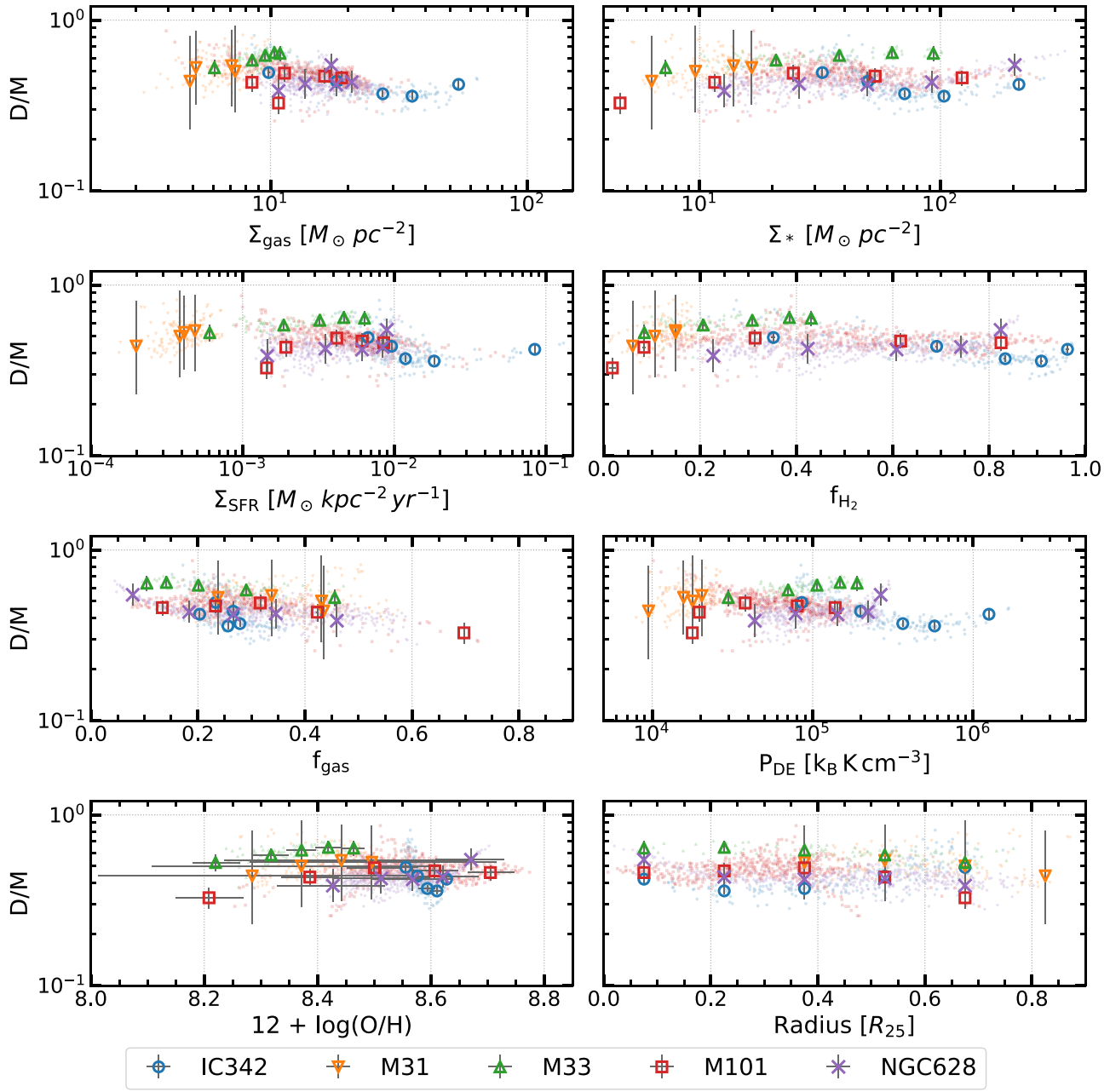

Figure 8. Relations between the physical quantities and D/M calculated with α_{CO}^{B13}. The variation of the D/M is minimum across all quantities displayed. Small symbols: pixel-by-pixel data where detection is above 3σ. Large symbols: average in radial bins. The error bar shows the 16th/84th percentile distribution from 1000 Monte Carlo tests, assuming a Gaussian error in the measurements.

ORCID iDs

I-Da Chiang (江宜達) https://orcid.org/0000-0003-2551-7148
Karin M. Sandstrom https://orcid.org/0000-0002-4378-8534
Jérémy Chastenet https://orcid.org/0000-0002-5235-5589
Cinthya N. Herrera https://orcid.org/0000-0001-6405-0785
Eric W. Koch https://orcid.org/0000-0001-9605-780X
Kathryn Kreckel https://orcid.org/0000-0001-6551-3091
Adam K. Leroy https://orcid.org/0000-0002-2545-1700
Jérôme Pety https://orcid.org/0000-0003-3061-6546
Dyas Utomo https://orcid.org/0000-0003-4161-2639
Thomas Williams https://orcid.org/0000-0002-0012-2142

References

Abdo, A. A., Ackermann, M., Ajello, M., et al. 2010, ApJ, 710, 133
Accurso, G., Saintonge, A., Catinella, B., et al. 2017, MNRAS, 470, 4750
Aniano, G., Draine, B. T., Gordon, K. D., & Sandstrom, K. 2011, PASP, 123, 1218
Aniano, G., Draine, B. T., Hunt, L. K., et al. 2020, ApJ, 889, 150
Aoyama, S., Hirashita, H., & Nagamine, K. 2020, MNRAS, 491, 3844
Asano, R. S., Takeuchi, T. T., Hirashita, H., & Inoue, A. K. 2013, EP&S, 65, 213
Asplund, M., Grevesse, N., Sauval, A. J., & Scott, P. 2009, ARA&A, 47, 481
Astropy Collaboration, Price-Whelan, A. M., Sipőcz, B. M., et al. 2018, AJ, 156, 123
Astropy Collaboration, Robitaille, T. P., Tollerud, E. J., et al. 2013, A&A, 558, A33
Berg, D. A., Pogge, R. W., Skillman, E. D., et al. 2020, ApJ, 893, 96

Berg, D. A., Skillman, E. D., Croxall, K. V., et al. 2015, ApJ, 806, 16
Bernstein, R. A., Freedman, W. L., & Madore, B. F. 2002, ApJ, 571, 56
Bolatto, A. D., Wolfire, M., & Leroy, A. K. 2013, ARA&A, 51, 207
Boquien, M., Calzetti, D., Combes, F., et al. 2011, AJ, 142, 111
Braun, R., Thilker, D. A., Walterbos, R. A. M., & Corbelli, E. 2009, ApJ, 695, 937
Bresolin, F. 2011, ApJ, 730, 129
Buat, V., Noll, S., Burgarella, D., et al. 2012, A&A, 545, A141
Calzetti, D. 2001, PASP, 113, 1449
Calzetti, D., Kennicutt, R. C., Engelbracht, C. W., et al. 2007, ApJ, 666, 870
Cazaux, S., & Tielens, A. G. G. M. 2004, ApJ, 604, 222
Chiang, I.-D., Sandstrom, K. M., Chastenet, J., et al. 2018, ApJ, 865, 117
Clark, C. J. R., De Vis, P., Baes, M., et al. 2019, MNRAS, 489, 5256
Clark, C. J. R., Schofield, S. P., Gomez, H. L., & Davies, J. I. 2016, MNRAS, 459, 1646
Compiègne, M., Verstraete, L., Jones, A., et al. 2011, A&A, 525, A103
Corbelli, E., Lorenzoni, S., Walterbos, R., Braun, R., & Thilker, D. 2010, A&A, 511, A89
Cormier, D., Bigiel, F., Jiménez-Donaire, M. J., et al. 2018, MNRAS, 475, 3909
Crosthwaite, L. P., Turner, J. L., & Ho, P. T. P. 2000, AJ, 119, 1720
Croxall, K. V., Pogge, R. W., Berg, D. A., Skillman, E. D., & Moustakas, J. 2016, ApJ, 830, 4
Dalcanton, J. J., Fouesneau, M., Hogg, D. W., et al. 2015, ApJ, 814, 3
De Cia, A., Ledoux, C., Mattsson, L., et al. 2016, A&A, 596, A97
De Cia, A., Ledoux, C., Petitjean, P., & Savaglio, S. 2018, A&A, 611, A76
De Vis, P., Gomez, H. L., Schofield, S. P., et al. 2017, MNRAS, 471, 1743
De Vis, P., Jones, A., Viaene, S., et al. 2019, A&A, 623, A5
Draine, B. T. 2003, ApJ, 598, 1017
Draine, B. T., Aniano, G., Krause, O., et al. 2014, ApJ, 780, 172
Draine, B. T., & Li, A. 2007, ApJ, 657, 810
Draine, B. T. 2009, in ASP Conf. Ser. 414, Cosmic Dust—Near and Far, ed. T. Henning, E. Grün, & J. Steinacker (San Francisco, CA: ASP), 453
Druard, C., Braine, J., Schuster, K. F., et al. 2014, A&A, 567, A118
Dwek, E. 1998, ApJ, 501, 643
Elmegreen, B. G. 1989, ApJ, 338, 178
Esteban, C., Peimbert, M., Torres-Peimbert, S., & Escalante, V. 1998, MNRAS, 295, 401
Fanciullo, L., Guillet, V., Aniano, G., et al. 2015, A&A, 580, A136
Feldmann, R., Gnedin, N. Y., & Kravtsov, A. V. 2012, ApJ, 747, 124
Fritz, J., Gentile, G., Smith, M. W. L., et al. 2012, A&A, 546, A34
Gallagher, M. J., Leroy, A. K., Bigiel, F., et al. 2018, ApJ, 858, 90
Galliano, F., Galametz, M., & Jones, A. P. 2018, ARA&A, 56, 673
Glover, S. C. O., & Clark, P. C. 2012, MNRAS, 421, 9
Glover, S. C. O., & Mac Low, M. M. 2011, MNRAS, 412, 337
Gordon, K. D., Roman-Duval, J., Bot, C., et al. 2014, ApJ, 797, 85
Gould, R. J., & Salpeter, E. E. 1963, ApJ, 138, 393
Gratier, P., Braine, J., Rodriguez-Fernandez, N. J., et al. 2010, A&A, 522, A3
Griffin, M. J., Abergel, A., Abreu, A., et al. 2010, A&A, 518, L3
Groves, B., Krause, O., Sandstrom, K., et al. 2012, MNRAS, 426, 892
Hildebrand, R. H. 1983, QJRAS, 24, 267
Hirashita, H. 1999, ApJL, 510, L99
Hirashita, H., & Aoyama, S. 2019, MNRAS, 482, 2555
Hirashita, H., & Kuo, T.-M. 2011, MNRAS, 416, 1340
Hou, K.-C., Aoyama, S., Hirashita, H., Nagamine, K., & Shimizu, I. 2019, MNRAS, 485, 1727
Hu, C.-Y., Zhukovska, S., Somerville, R. S., & Naab, T. 2019, MNRAS, 487, 3252
Hunt, L. K., García-Burillo, S., Casasola, V., et al. 2015, A&A, 583, A114
Hunter, J. D. 2007, CSE, 9, 90
Inoue, A. K. 2003, PASJ, 55, 901
Israel, F. P. 1997, A&A, 328, 471
Israel, F. P. 2020, A&A, 635, A131
Issa, M. R., MacLaren, I., & Wolfendale, A. W. 1990, A&A, 236, 237
Jenkins, E. 1989, in IAU Symp. 135, Interstellar Dust, ed. L. J. Allamandola & A. G. G. M. Tielens (Berlin: Springer), 23
Jenkins, E. B. 1987, Element Abundances in the Interstellar Atomic Material, Vol. 134 (Dordrecht: Reidel), 533
Jenkins, E. B. 2009, ApJ, 700, 1299
Jenkins, E. B. 2014, arXiv:1402.4765
Jenkins, E. B., & Wallerstein, G. 2017, ApJ, 838, 85
Jones, A. P., Köhler, M., Ysard, N., Bocchio, M., & Verstraete, L. 2017, A&A, 602, A46
Joye, W. A., & Mandel, E. 2003, in ASP Conf. Ser. 295, Astronomical Data Analysis Software and Systems XII, ed. H. E. Payne, R. I. Jedrzejewski, & R. N. Hook (San Francisco, CA: ASP), 489
Kennicutt, R. C., Calzetti, D., Aniano, G., et al. 2011, PASP, 123, 1347
Kennicutt, R. C., & Evans, N. J. 2012, ARA&A, 50, 531
Kerp, J., Winkel, B., Ben Bekhti, N., Flöer, L., & Kalberla, P. M. W. 2011, AN, 332, 637
Kewley, L. J., & Ellison, S. L. 2008, ApJ, 681, 1183
Koch, E. W., Rosolowsky, E. W., Lockman, F. J., et al. 2018, MNRAS, 479, 2505
Kramer, C., Buchbender, C., Xilouris, E. M., et al. 2010, A&A, 518, L67
Kreckel, K., Ho, I. T., Blanc, G. A., et al. 2019, ApJ, 887, 80
Krumholz, M. R., Leroy, A. K., & McKee, C. F. 2011, ApJ, 731, 25
Lang, P., Meidt, S. E., Rosolowsky, E., et al. 2020, ApJ, 897, 122
Leroy, A. K., Bolatto, A., Gordon, K., et al. 2011, ApJ, 737, 12
Leroy, A. K., Sandstrom, K. M., Lang, D., et al. 2019, ApJS, 244, 24
Leroy, A. K., Walter, F., Bigiel, F., et al. 2009, AJ, 137, 4670
Leroy, A. K., Walter, F., Brinks, E., et al. 2008, AJ, 136, 2782
Leroy, A. K., Walter, F., Sandstrom, K., et al. 2013, AJ, 146, 19
Li, Q., Narayanan, D., & Davé, R. 2019, MNRAS, 490, 1425
Lisenfeld, U., & Ferrara, A. 1998, ApJ, 496, 145
Lodders, K. 2003, ApJ, 591, 1220
Ma, X., Hopkins, P. F., Faucher-Giguère, C.-A., et al. 2016, MNRAS, 456, 2140
Makarov, D., Prugniel, P., Terekhova, N., Courtois, H., & Vauglin, I. 2014, A&A, 570, A13
Martin, D. C., Fanson, J., Schiminovich, D., et al. 2005, ApJL, 619, L1
McKinney, W. 2010, in Proc. Python in Science Conf. 9: SciPy 2010, ed. S. van der Walt & J. Millman (Austin, TX: SciPy), 51
McMullin, J. P., Waters, B., Schiebel, D., Young, W., & Golap, K. 2007, in ASP Conf. Ser. 376, Astronomical Data Analysis Software and Systems XVI, ed. R. A. Shaw, F. Hill, & D. J. Bell (San Francisco, CA: ASP), 127
McQuinn, K. B. W., Skillman, E. D., Dolphin, A. E., Berg, D., & Kennicutt, R. 2017, AJ, 154, 51
Nieten, C., Neininger, N., Guélin, M., et al. 2006, A&A, 453, 459
Peimbert, A., & Peimbert, M. 2010, ApJ, 724, 791
Péroux, C., & Howk, J. C. 2020, ARA&A, 58, 363
Pilbratt, G. L., Riedinger, J. R., Passvogel, T., et al. 2010, A&A, 518, L1
Pilyugin, L. S., & Grebel, E. K. 2016, MNRAS, 457, 3678
Planck Collaboration, Ade, P. A. R., Aghanim, N., et al. 2016, A&A, 586, A132
Poglitsch, A., Waelkens, C., Geis, N., et al. 2010, A&A, 518, L2
Reach, W. T., Dwek, E., Fixsen, D. J., et al. 1995, ApJ, 451, 188
Relaño, M., Lisenfeld, U., Hou, K. C., et al. 2020, A&A, 636, A18
Rémy-Ruyer, A., Madden, S. C., Galliano, F., et al. 2014, A&A, 563, A31
Roman-Duval, J., Aloisi, A., Gordon, K., et al. 2019a, BAAS, 51, 458
Roman-Duval, J., Bot, C., Chastenet, J., & Gordon, K. 2017, ApJ, 841, 72
Roman-Duval, J., Gordon, K. D., Meixner, M., et al. 2014, ApJ, 797, 86
Roman-Duval, J., Jenkins, E. B., Williams, B., et al. 2019b, ApJ, 871, 151
Rots, A. H. 1979, A&A, 80, 255
Rowlands, K., Gomez, H. L., Dunne, L., et al. 2014, MNRAS, 441, 1040
Sandstrom, K. M., Leroy, A. K., Walter, F., et al. 2013, ApJ, 777, 5
Schruba, A., Leroy, A. K., Kruijssen, J. M. D., et al. 2017, ApJ, 835, 278
Schruba, A., Leroy, A. K., Walter, F., et al. 2012, AJ, 143, 138
Schwartz, P. R. 1982, ApJ, 252, 589
Sofue, Y., Tutui, Y., Honma, M., et al. 1999, ApJ, 523, 136
Solomon, P. M., Rivolo, A. R., Barrett, J., & Yahil, A. 1987, ApJ, 319, 730
Strong, A. W., & Mattox, J. R. 1996, A&A, 308, L21
Sun, J., Leroy, A. K., Ostriker, E. C., et al. 2020, ApJ, 892, 148
Tully, R. B., Rizzi, L., Shaya, E. J., et al. 2009, AJ, 138, 323
van der Walt, S., Colbert, S. C., & Varoquaux, G. 2011, CSE, 13, 22
Vílchez, J. M., Relaño, M., Kennicutt, R., et al. 2019, MNRAS, 483, 4968
Walter, F., Brinks, E., de Blok, W. J. G., et al. 2008, AJ, 136, 2563
Winkel, B., Kerp, J., Flöer, L., et al. 2016, A&A, 585, A41
Wolfire, M. G., Hollenbach, D., & McKee, C. F. 2010, ApJ, 716, 1191
Wright, E. L., Eisenhardt, P. R. M., Mainzer, A. K., et al. 2010, AJ, 140, 1868
Wu, P.-F., Tully, R. B., Rizzi, L., et al. 2014, AJ, 148, 7
Xilouris, E. M., Tabatabaei, F. S., Boquien, M., et al. 2012, A&A, 543, A74
Yamasawa, D., Habe, A., Kozasa, T., et al. 2011, ApJ, 735, 44
Zhukovska, S. 2014, A&A, 562, A76
Zhukovska, S., Dobbs, C., Jenkins, E. B., & Klessen, R. S. 2016, ApJ, 831, 147
Zhukovska, S., Gail, H.-P., & Trieloff, M. 2008, A&A, 479, 453
Zurita, A., & Bresolin, F. 2012, MNRAS, 427, 1463